CHALMERS
UNIVERSITY OF TECHNOLOGY

Numerical Simulation of Cavitation on a Tidal Turbine using ReFRESCO

URANS Modeling of the Southampton HATT

Master's Thesis in the International Master's Programme Naval Architecture and Ocean Engineering

BEHRAD GHARRAEE

Numerical Simulation of Cavitation on a Tidal Turbine using ReFRESCO

URANS Modeling of the Southampton HATT

BEHRAD GHARRAEE

Numerical Simulation of Cavitation on a Tidal Turbine using ReFRESCO
URANS Modeling of the Southampton HATT
BEHRAD GHARRAEE

Cover image: Vortical field visualization and cavitation identification of the Southampton Horizontal Axis Tidal Turbine.

Numerical Simulation of Cavitation on a Tidal Turbine using ReFRESCO
URANS Modeling of the Southampton HATT

BEHRAD GHARRAEE
Department of Shipping and Marine Technology
Division of Marine Technology
Chalmers University of Technology

Abstract

As renewable energies continue to grow their share in the global energy landscape, marine resources present an inexhaustible potential to provide the ever increasing human settlements energy demands. Tidal energy conversion technologies enjoy the benefits of the accurately predictable and highly reliable resources, while promising great power to weight ratio due to the relatively small size of the equipment compared with offshore wind for instance.

There are various prototypes being tested today and some proposals are employing floating structures as the platform for the energy converters, the design of which is driven by the higher kinetic energy content of the streams close to the water surface. Such concepts increase the turbines susceptibility to cavitation. There has been very little explicit research performed on the cavitation behavior of tidal turbines and this thesis attempts to establish one such study to enable and promote future investigations.

The specialized hydrodynamic RANS solver ReFRESCO is used with the built-in Sauer cavitation model. Structured grids have been employed. The effectiveness of an eddy-viscosity modification method known as the Reboud correction is also subject of investigation for improving dynamic behavior of cavities. Two different turbulence models used are k-ω (SST-2003) and k-$\sqrt{k}L$.

A three-bladed model scale Horizontal Axis Tidal Turbine (HATT) is numerically simulated in open-water conditions in an attempt to reproduce previous EFD results from the University of Southampton, thus validating the numerical procedures in use. The simulations are performed through three stages where initially a steady solution is obtained, then the simulation becomes transient and finally the cavitation model is switched on.

The results are validated against experiments via non-dimensionalized parameters for thrust and torque, which prove satisfactory. General flow shows good agreement with experimental observations and the cavity formation appears to be accurate regarding both its position and blade coverage. Interestingly a cavity is observed near the leading edge on the pressure side. The simulations fail to resolve the details near the closure line of the sheet cavity which is attributed to inadequate meshing resolution. Very little dynamic behavior of the cavity structure is observed specifically where a "horse-shoe" cavity structure had been detected during EFD, which will be subject to future work.

Keywords: Tidal Turbines, Cavitation, CFD, URANS, ReFRESCO, Renewable Energy, Marine Currents

Acknowledgements

Table of Contents

List of Figures

List of Tables

List of Symbols

Acronyms

Symbol	Description
AFM	Absolute Formulation Method
ALE	Arbitrary Lagrangian-Eulerian
BC	Boundary Condition
BEM	Blade Element Method
BP	British Petroleum
BV	Bureau Veritas
C^3SE	Chalmers Centre for Computational Science and Engineering
CFD	Computational Fluid Dynamics
$CGNS$	CFD General Notation System
$DDES$	Delayed Detached-Eddy Simulation
DES	Detached-Eddy Simulation
DNS	Direct Numerical Simulation
$DNV\ GL$	Det Norske Veritas Germanischer Lloyd
EFD	Experimental Fluid Dynamics
$EMEC$	European Marine Energy Centre
GHG	Green House Gas
$HATT$	Horizontal Axis Tidal Turbine
HPC	High-Performance Computing
LES	Large Eddy Simulation
$MARIN$	Maritime Research Institute Netherlands

MCT	Marine Current Turbine
MPI	Message Passing Interface
MVG	Moving Grid
$PANS$	Partially Averaged Navier Stokes
PDE	Partial Differential Equation
$QUICK$	Quadratic Upstream Interpolation for Convective Kinematics
$RANS$	Reynolds-Averaged Navier-Stokes
RE	Richardson Extrapolation
$ReFRESCO$	Reliable & Fast RANS Equations (solver for) Ships, Cavitation (and) Offshore
RFM	Relative Formulation Method
RPM	Revolutions Per Minute
SAS	Scale Adaptive Simulation
$SIMPLE$	Semi-Implicit Method for Pressure Linked Equations
TEC	Tidal Energy Convertor
TSR	Tip Speed Ratio
$URANS$	Unsteady Reynolds-Averaged Navier-Stokes
$VATT$	Vertical Axis Tidal Turbine
VOF	Volume of Fluid

Greek Alphabet

Symbol	Description
α_i	Phase fraction
δ_{ij}	Kronecker's delta
ϵ	Error estimator
ϵ	Turbulent dissipation
μ	Dynamic viscosity
μ_i	Partial viscosity
μ_l	Molecular viscosity

xviii

μ_t	Turbulent (eddy) viscosity
∇	Gradient operator
ν	Shedding frequency
ω	Angular velocity
Ω_{ij}	Anti-symmetrical velocity gradient tensor
ρ	Mass density
ρ_i	Partial density
σ	Cavitation number
σ_{ij}	Normal stress tensor
τ_{ij}	Shear stress tensor

Roman Letters

Symbol	Description
$\bar{F}$	Sum of pressure, viscous and external forces
$\mathbf{U}$	Velocity vector
Ω_{ij}	Vorticity tensor
A	Rotor area
c/R	Chord length to maximum radius ratio
C_μ	Turbulent viscosity constant
C_L	Sectional lift coefficient
C_P	Power coefficient
C_T	Thrust coefficient
$C_{p,min}$	Minimum pressure coefficient
D_{ij}	Velocity gradient tensor
f_i	Force
k	Turbulent kinetic energy
L	Characteristic Length
L_2	RMS residual norm
L_{inf}	Infinity residual norm

n	Reboud density damping factor
n	Rotational speed
n_0	Initial cavity nuclei concentration
P	Pressure
P'	Instantaneous pressure fluctuation
P, Q, R	Velocity gradient tensor invariants
P_0	Absolute free stream pressure
P_l	Local pressure
P_v	Vapor saturation pressure
Q	Torque
Q_v	Vapor production term
Q_{α_i}	Partial phase production term
r	Local radius
r/R	Local radius to maximum radius ratio
R_0	Initial cavity nuclei radii
Re	Reynolds number
S_{ij}	Symmetric velocity gradient (rate of strain) tensor
St	Strouhal number
T	Thrust
t	Time
t/c	Thickness to chord length ratio
U	Characteristic velocity
U_T	Tunnel inflow velocity
V	Velocity
v_i'	Instantaneous velocity fluctuation
v_i, v_j, v_k	Cartesian velocity components
V_{ref}	Reference velocity at tunnel inflow
V_{res}	Localized resultant velocity
x_i, x_j, x_k	Cartesian coordinates

1

Introduction

Population growth and energy production are two of the leading factors in determining an energy outlook for the world. At current growth rates and within the next two decades, energy demand will not be balanced out by the supply (British Petroleum, 2014). This imbalance results in an energy deficit that may be the cause of much burden placed on the future generations which will inherit a lifestyle of consuming too much energy, supplied from too little resources. Combined with the growing public consciousness of environmental sustainability, global concerns for the catastrophic consequences of man-made climate change can bring the ideal of a CO_2-neutral energy cycle closer to reality. BP have forecast that the rate of growth of carbon emissions will slow from 2.5% to 0.7% between 2013 and 2035, but will remain net positive, indicating that more needs to be done in order to keep the total tonnage of carbon footprint below that recommended by the scientific community (British Petroleum, 2014).

1.1   Ocean Renewable Energy

Energy resources that are naturally replenished on a human timescale are called *renewables*. The Earth is a lively, dynamic planet and has been transforming energy for a long time. Resources such as plants, geothermal, wind, sunlight, waves, tides and rain all carry energy that can be extracted by means of technology. Contrary to Green House Gas (GHG)-emitting fossil fuels, these resources can be sustained for an infinite period of time; they are virtually inexhaustible[1].

While expanding at a rate more than that of other energy sources, renewables are still shaping only a small fraction of the energy supply landscape perhaps as a result of the relative young age of the industry. From a commercial point of view the infrastructure that needs to be in place is still lacking for many of these technologies. Ocean renewables present nonetheless an excellent opportunity to harvest the massive resources that exist in offshore wind, wave and tidal. The focus of attention here will be on tidal energy.

1.2   Tidal Energy

Intermittency is by far the leading downside of renewable energy sources i.e., power is not always generated when it is needed, and when power is generated it is not

---

[1]In case of plants the condition is that they are cultivated in a sustainable manner.

necessarily needed. This combined with the fact that most renewable energy sources are not storable makes for major logistic challenges. Tidal energy is from a practical point of view, most competitive when it comes to predictability when in fact for all the many square meters of solar panels already laid down, the solar energy sector is still dependent on favorable weather; without clear skies there is no solar energy. Wind powered turbines suffer similarly from unfavorable weather conditions, there is always the threat of calm skies. Tidal energy on the other hand is predictable to 98% of accuracy for decades (Elghali et al., 2007).

Tides are not only predictable, but also reliable since they arise from the relative arrangement of the masses of Earth, the Moon and the Sun, which is believed to remain rather stable for the next few millions of years[2]. As long as these three celestial bodies maintain their current arrangement, the oceans and waterways will sustain tidal currents, and many coastlines will experience these currents twice daily predictable down to the minutes[3].

In addition to being predictable and reliable, tidal energy is in an advantage over wind energy since a marine turbine will extract more energy compared to a wind turbine of the same size from the same amount of incoming flow. The density of the incoming fluid (seawater) which is about 800 times larger than air is responsible for this difference in kinetic energy (Elghali et al., 2007).

Although thermal and density gradient effects contribute to the marine currents on earth, the prominent driver behind such streams are the tides. Occurrence and magnitude of tides is a function of the distance of the Moon and the Sun to the earth. These two celestial bodies affect the tides on Earth's waters in a combination of different ways. In addition, the maximum current velocities during lunar revolution cycles, water depth, 50 years wave-height, significant wave-height and proximity to land determine the energy potential of the tides. The interested reader is referred to Elghali et al. (2007) for a foundation on tidal energy conversion.

One of major downsides to tidal energy is the limited presence of economically justified tidal fields around the globe. This resources harvesting capacity is further limited by the non-continuous nature of the tidal surges which at best occur at 10-12 hour intervals. The impact of rotating machinery on the safety and well-being of marine life is a concern that needs to be addressed on a case-by-case basis. Due to the harsh subsea working conditions this technology is more prone to maintenance-related downtime compared with wind or solar.

1.2.1 Tidal Resources

Past

The first fully commercialized tidal power generation plant (although technologically different from HATTs) was established some 50 years ago in 1966 at the estuary of the Rance River, in Brittany, France. While it may be more of a tourist attraction

---

[2]This is in fact a subject of discussion between astronomers but for the purpose of engineering applications which rarely foresee time-spans beyond centuries, proofs of the stability of the solar system have been developed already in the time of Lagrange (Moser, 1978).

[3]The most common type are semidiurnal tides. Diurnal and mixed tides exist depending among other factors on the latitude of the coastline.

because of its relatively small share in the consumers market, *La Rance Barrage* is an indication of the heritage of renewable energy sources in practice.

Since then the development of tidal and similar technologies have been hindered due to the excessively low price of fossil fuels. However in recent decades with rising oil prices as well as the environmental consequences of burning hydrocarbons for energy purposes, there is once again a well-backed initiative to revise and improve sustainable energy sources. The political instability of many oil producing regions in the world is another major driving force for independence from fossil fuels.

Present

While in no position to make economic forecasts, the author wishes to add that in recent months oil prices have demonstrated a substantial drop which is not likely to be an indication of the decline of the petroleum industry as a whole but rather a transient situation caused primarily by the aforementioned political instabilities. There have been at least two major similar oil price drops within the past three decades and the current trend is understood to eventually reverse as did its predecessors. That being said, the petroleum industry is unlikely to transform internally and make room for emerging energy sources. This needs to be orchestrated by external organizations, institutions and regulators so that short-term thinking can not hinder the long-term investments that are needed in order to mature such a young but rapidly growing industry.

Global tides are estimated to hold a capacity of 100 GW installed power. Unfortunately this massive and predictable energy source is not available worldwide. Only certain waters harbor the potential for tides and that is from a power distribution point of view, challenging. Where it does exist however, for example in the UK, tidal energy can provide potentially an estimated 18 TWh/year which adds up to 5% of the country's energy demand (Hardisty, 2008). With an off-grid mindset of how power should be produced and transported, it can already benefit local communities a great deal.

State of the art in terms of power production per turbine is at the time of this thesis 2.5 MW from a stream at $4.0[m/s]$ which is the rated power of the *D15* model from French developer *Sabella*. A Chinese state-owned prototype tidal generator with rated power of 3.4 MW has been deployed very recently off the island of Zhoushan for testing and is expected to start generating an annual output of 6,000 MWh by June, 2016.

There exists a trend of deploying "tidal farms" comprised of multiple smaller turbines instead of a single larger turbine on the grounds that excessively large turbines will not be cost effective to manufacture and maintain (Carbon Trust, 2011). If such deployment strategies prevail, the ceiling for projected megawatts will be virtually non-existent.

Future

As valuable as local consumers are, whether the tidal turbines can be used locally is irrelevant. Such is the case with petroleum and similar energy carriers, where the product can be transported rendering it an issue of logistics for the technology

developers. To have the infrastructure in place for when the market demand surfaces, is the success factor. It is an interesting time with government and inter-government funds and subsidies in the millions of Euros flowing into various renewable energy startups and research institutes. The same is happening with implementation and safety protocols from classification societies (most recently from BV and DNV GL) as the finalized versions are just being published.

Fortunately the trend has been set for major oil companies to initiate within their R&D departments a (still small but valuable) renewables division. It is not at all unimaginable that in the long run these renewable divisions will grow to shape a large part of the profit that goes into the companies at which point the idea of halting fossil fuel excavation can be deemed not so Utopian. This just might be the dawn of the age of commercialized marine renewable energy.

1.2.2 Technology Concepts

A Tidal Energy Converter (TEC) can be categorized under six different types based on the working principle according to EMEC (2015):

- Horizontal Axis Tidal Turbines (HATT): The tidal stream rotates the blades around the horizontal axis thus generating power. These resemble underwater wind turbines. See Figure 1.1a (MCT, 2011).

- Vertical Axis Tidal Turbines (VATT): These turbines employ the same concept as HATTs but unlike HATTs they are mounted on a vertical axis. The tidal stream causes the blades to rotate around the vertical axis. See Figure 1.1b (ESRU, 2006).

- Oscillating Hydrofoil: In this type of device a hinged arm with a hydrofoil attached to one end oscillates by the lift forces caused by the stream on the hydrofoil. A hydraulic system then converts the energy of this motion to electricity. See Figure 1.1c (Harris, 2012).

- Enclosed Tips (Venturi): By employing the Venturi Effect, these devices subject the hydro-turbine to the concentrated flow through the duct and magnify flow velocity. See Figure 1.1d (Harris, 2012).

- Archimedes Screw: A helical cork-screw shaped device is mounted on an inclined central shaft and draws power from the stream through the flow of water up and around the spiral. See Figure 1.1e (Flumill AS, 2012).

- Tidal Kite: Much like an underwater kite, which has a turbine attached to it, this device completes its rounds on an infinity symbol-shaped (∞) path thus increasing the speed of water inflow to the turbine. See Figure 1.1f (Minesto AB, 2011).

Other types of devices which employ very unique designs and working principles also exist that do not fall under these recognized categories.
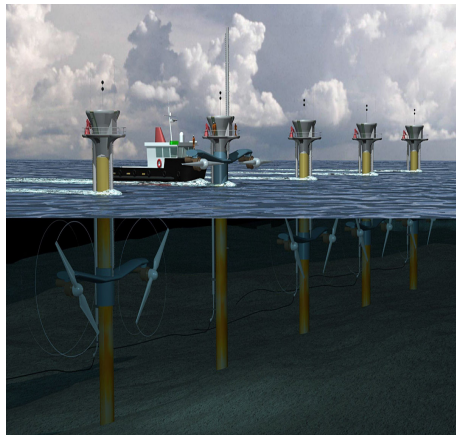
(a) HATT
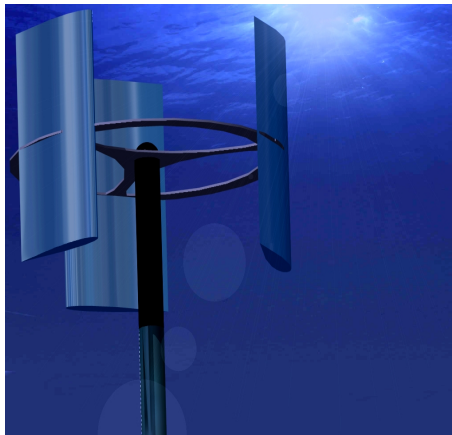
(b) VATT
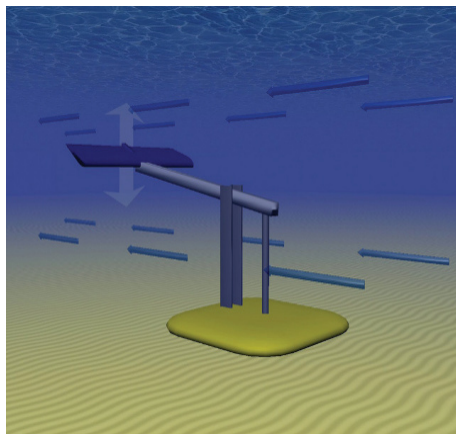
(c) Oscillating Foil
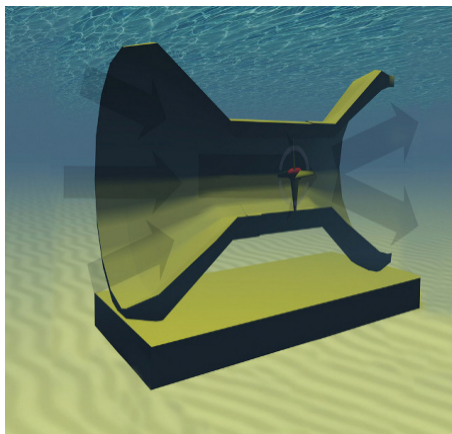
(d) Venturi
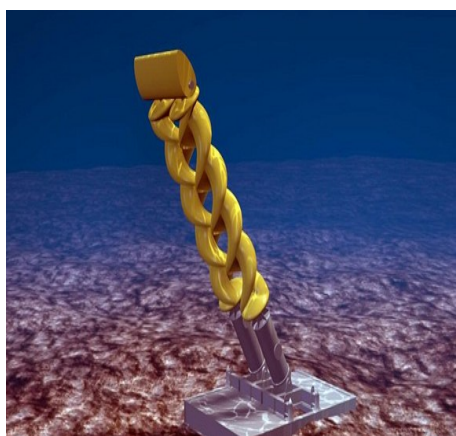
(e) Archimedes Screw
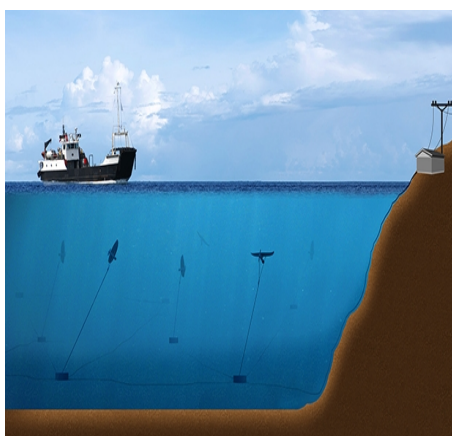
(f) Tidal Kite

Figure 1.1: Tidal energy converters categorized according to EMEC (2015).

1.2.3 Fixture Methods

The TECs are further categorized based on their method of fixing on site:

- Seabed Mounted / Gravity Base: Either by attaching the turbine to seabed or allowing it to rest on the seabed due to its massive weight, this technology can be combined with mooring lines.

- Pile Mounted: Much like what is done with large wind turbines the device is mounted on a pole that has penetrated the ocean floor. If a horizontal axis device is used with this type of mounting, it is possible to allow the turbine to yaw around the vertical axis. The pole could also be used to lift up the turbine for maintenance above water level.

- Floating: There can be three ways to float a turbine structure:

  - Flexible mooring: Using subsea cables the device is moored to the seabed and allowed to swing with the direction of the stream.

  - Rigid mooring: The connection lines are rigid and allow very little movement.

  - Floating structure: An array of turbines may be mounted on a floating structure where the floating structure itself can move relatively freely, moving the entire array of turbines with it. See Figure 1.2.

(a)   (b)
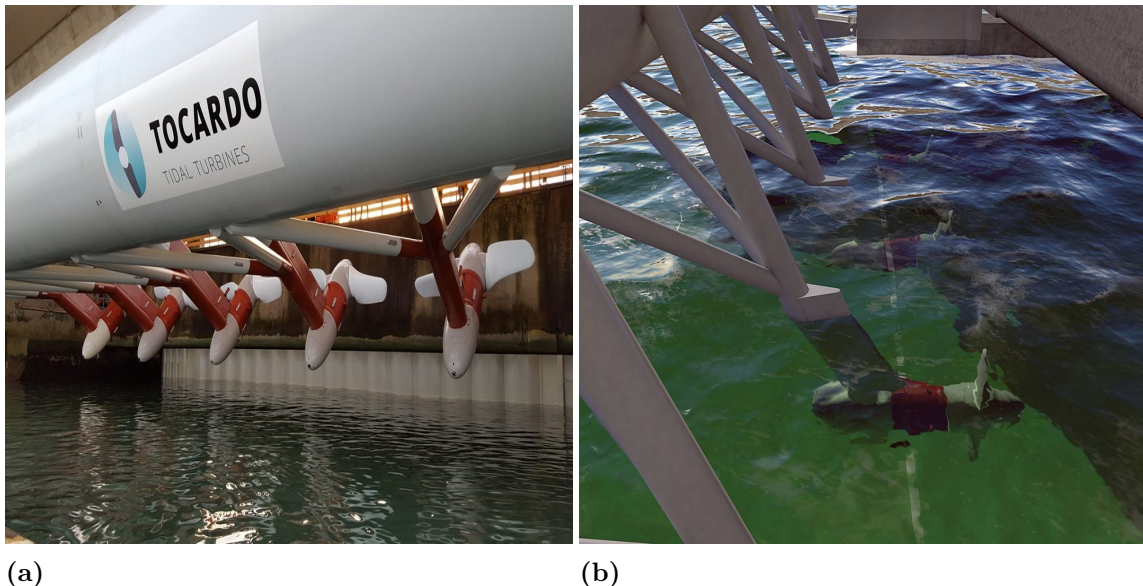
Figure 1.2: (a) Array of Tocardo turbines mounted on a floating structure (Tidal Energy Today, 2015a), (b) turbines lowered into the water, maintaining close proximity to the surface (Tidal Energy Today, 2015b). This raises concerns regarding cavitation.

- Hydrofoil Inducing Downforce: By mounting multiple hydrofoils on the frame, this structure uses the downforce generated by the hydrofoils to secure itself to the seabed, provided that the sectional area is sufficient to counteract the overturning moment.

1.3 Literature Survey

HATT experimental studies

A comprehensive series of tests have been performed in the towing tank and cavitation tunnel of the University of Southampton by Bahaj et al. (2007) on a reference turbine. These included parametric studies of immersion depth, inflow velocity, turbine rotational velocity, cavitation number and blade pitch among other factors, results of which are used herein in the form of Figure 3.3. The non-dimensionalized values defined in consistence with the experiments are described below. Newcastle University (Shi et al., 2015), University of Newcastle upon Tyne (Wang et al., 2007) and the University of Manchester (Mcnaughton, 2013) have also performed their independent tests on other similar turbines.

Numerical studies on the Southampton turbine

The Southampton turbine has been the subject of numerical studies with emphasis on different operational aspects. Wetted flow Reynolds-Averaged Navier-Stokes (RANS) and Large Eddy Simulation (LES) computations of Afgan et al. (2013) and LES computations of McNaughton et al. (2014) have been performed where the fluid structure interactions including the turbine mast were subject of investigation. Turnock et al., (2011) use coupled BEM-RANS modeling to study the wake of an array of tidal turbines. In Lloyd et al., (2011b) the CFD library Open-FOAM is used to make power predictions with Unsteady Reynolds-Averaged Navier-Stokes (URANS). Banks et al., (2013) also uses Blade Element Method (BEM) and LES to study fluid structure interactions. Noise generation of the tidal turbine is the subject of studies in Lloyd et al., (2011a).

There has also been simulations performed on the Southampton turbine using ReFRESCO which is the code used also in this thesis and further introduced in Section 2.5. The direct predecessor of the present research is the Otto et al., (2012) studies, in which steady RANS simulations of the turbine were performed without taking into account the cavitation phenomenon. It was originally proposed in that paper that this be performed as future work. The Lampe (2015) internal report contains valuable experiences with regards to using the structured GridPro mesh used also herein, although only wetted flow simulations were performed therein. The poor convergence behavior of that study is a target for improvement in the present thesis.

Non-dimensional analysis

The Tip Speed Ratio (TSR), thrust (C_T) and power (C_P) coefficients are used frequently in the present report when referring to experimental and numerical results and are non-dimensionalized as

$$TSR = \frac{\omega R}{U_T}, \quad C_T = \frac{T}{\frac{1}{2}\rho U_T^2 A}, \quad C_P = \frac{Q\omega R}{\frac{1}{2}\rho U_T^3 A} \qquad (1.1)$$

where $\omega[rad/s]$ is angular velocity[4], $R[m]$ is rotor radius, $U_T[m/s]$ is tunnel inflow velocity, $T[N]$ is thrust loading in x-direction for three blades, $Q[N.m]$ is torque with reference to the x-axis and $A[m^2]$ is the rotor diameter area defined as πR^2.

1.4 Significance of Cavitation in HATTs

As noted above, some applications propose the concept of fixing the tidal turbines on a hanging structure connected to floating platforms. This proximity to the water surface introduces risks of additional cavitation on the blades. Given the emergence of such concepts, a solid study on the cavitating characteristics of the tidal turbines seems justified, if not overdue. It is conceived that there exists a "cavitation safe" region where the hydrostatic pressure is high enough and distance to sea bed is large enough to avoid harmful interactions.

Cavitation is associated with thrust reduction, erosion, vibration and noise all of which need to be carefully investigated in conventional propeller designs for example. The presence of the support structure which would suffer from the pressure pulses and erosiveness of tip vortex cavitation calls for an investigation into these formations. Cavities which form and collapse on the blade surface can cause efficiency and stability degradation in the life cycle of the turbine and thus need to be avoided as much as possible.

To the best of the authors knowledge at the time of writing, there has been very little URANS studies on the cavitation of HATTs. Huang et al., (2015) studied cavitation inception on a counter-rotating HATT setup using the solver CFX14.0. Lee et al., (2012) performed a design process for the turbine blades with cavitation inception delay in focus. But for the majority of such simulations, the cavitation phenomenon is neglected.

The lack of interest in cavitating HATTs is likely a result of their deep water applications where with ample hydrostatic pressure concerns over cavitation are more or less alleviated. Floating support structure concepts however intrigue the scientific mind to determine whether cavitation truly is a non-issue. The author is thereby convinced that such an investigation should be initiated at the early stages as to reduce design alterations later on in the development of the turbines.

---

[4]Not to be mistaken with *rotational speed* (n) with dimensions [rps], [rpm] or [Hz] which is used for non-dimensionalization of pressure.

1.5 Objective and Scope of Work

The general goal is to simulate cavitating flow around a HATT using URANS methods. Simulations will be carried out using the viscous-flow solver ReFRESCO with a built-in cavitation model. A standard HATT setup will be investigated under different flow velocities and rotational speeds. Analysis will focus on cavitation inception and cavitation dynamics. Of special interest would be to investigate which parameters yield the horse-shoe cloud cavity reported in Bahaj et al., (2007), as this type of cavity is often highly erosive. Furthermore the reproduction of this specific cavity form will contribute immensely to the validation of the numerical procedure. In summary the objectives are to:

1. Reproduce wetted flow calculations by Otto et al., (2012) using the new version of ReFRESCO and the new structured grid generated by Lampe (2015),

2. Perform verification study by using these structured grids in steady wetted flow condition,

3. Perform unsteady wetted flow calculations and compare with steady results,

4. Perform validation against experiments,

5. Perform unsteady cavitating flow calculations and compare with experiments,

6. Analyze flow field details both for wetted and cavitating flow calculations.

1.5.1 Limitations

There are several aspects of the Experimental Fluid Dynamics (EFD) tests that are not preserved in the simulations. The cross section of the cavitation tunnel which will influence pressure on the blades especially closer to the tip has not been taken into account as is shown in Figure 3.8. Furthermore the blade geometries have been modified as explained in Section 3.2.

The effects of gravity acceleration and density variations thereof have been omitted. Free surface effects are also not included as a result of the large immersion depth. There are no full scale Reynold's number tests performed herein.

1.6 Report Layout

Chapter 2 will delve deeper into the mathematical foundations behind the used turbulence and cavitation models as well as their physical definitions. The CFD solver ReFRESCO is introduced and methods for capturing flow properties like vortices and cavitation dynamics are explained. The chapter is concluded by an outline of the performed numerical computations. In Chapter 3 the experimental setup and findings are summarized and the numerical setup will be presented including grid details and Boundary Condition (BC) settings. In Chapter 4 a formal verification study is performed including grid refinement analysis. The numerical uncertainties

attained thereof are later used in the presentation of results in Chapter 5 where various findings from the simulations are reported. Finally Chapter 6 will summarize the report and propose beneficial expansions for future work.

Although the report is carefully cross referenced for the non-sequential reader, it is recommended to proceed with the chapters in the presented order. The reader is presumed to have some familiarity with the basic concepts of cavitation, turbulence and its modeling. References do however exist throughout the text in order to aid the interested reader in extending their knowledge of the mechanical principles of turbulent flow.

2
Numerical Methodology

This chapter explains the underlying physics of turbulent flow and cavitation, then proceeds to introduce their numerical modeling and the techniques that are used for solving these models.

2.1 Turbulence

In the absence of a unanimous definition for turbulent flow one must resort to some of the characteristics of flow to identify turbulence, which are (Davidson, 2011):

1. Irregularity: *Not* to be confused with randomness, turbulent flow exhibits chaotic behavior. Different length and velocity scales of eddies do exist within any given region of a turbulent flow for limited periods of time. These various eddy scales contribute to what is known as the cascade process (see Dissipation) responsible for the transfer of kinetic energy from the main flow into the smallest scales of turbulence. This behavior although chaotic, is governed by the Navier-Stokes Equation.

2. Diffusivity: Due to the eventful nature of turbulent flow, it is highly efficient in diffusing fluid properties such as its momentum, friction and heat transfer.

3. High Reynold's Numbers: While it is difficult to draw a precise line with regards to turbulence initiation, it is generally understood to appear in high Reynold's number values.

4. Three-dimensionality: Turbulent flow is always unsteady and three dimensional even for 2D bodies.

5. Dissipation: Turbulence ultimately generates heat from the kinetic energy of the mean flow. This is materialized by the subsequent transfer of kinetic energy from the largest eddies to the smallest where it is finally transformed into internal energy i.e., heat. This is known as the cascade process.

6. Continuum: Even the smallest eddy structures are sufficiently larger than the molecular scale to allow the flow to be treated as a continuum.

2.2 Basic Cavitation Theory

Existence of gas cavities within an otherwise single phase fluid is for the majority of engineering applications considered an adverse phenomenon. The origins of

cavitation are generally traced to the local thermodynamic characteristics of the continuous medium in liquid phase, namely pressure and temperature among other parameters. Cavitation is similar to boiling in that both are thermodynamic processes in which the liquid phase changes to gas phase. The difference being that boiling occurs due to an increase in the local vapor pressure of the liquid that is sufficient to surpass the ambient pressure thus enabling the phase change. In case of cavitation, the liquids local pressure must fall (likely under an adiabatic process) below that of the vapor saturation pressure at the ambient temperature, so that the tensile strength of the liquid can no longer maintain a liquid phase, analogous to a rupture in the liquid continuum.

In simpler terms, a drop in local fluid pressure below that of the saturated vapor pressure which is primarily a function of temperature, will under certain circumstances result in cavitation nucleation. The *nuclei* are of the smallest possible diameter of a gaseous sphere that the liquids surface tension allows. If cavitating conditions are sustained over a relatively long period of time (in the order of a second) the nuclei are permitted to grow and develop into various known forms of cavities. Generally, the conditions that are required to sustain cavity nuclei are a mechanical equilibrium between the internal pressure of the cavity caused by the gas' partial pressure and the surface tension of the "micro-bubble".

One common mechanism through which the nuclei may grow to become bubble cavities is the transition of the nuclei through a region of low pressure where they will maintain equilibrium and undergo a diameter increase. There exist a range of cavity formations which behave rather differently from one another. Franc and Michel (2006) categorizes these as:

- *Bubble cavities* which frequently appear at the point of inception for regions of isolated low pressure.

- *Sheet cavities* cover extended regions of low pressure on the surface of the body. These are further categorized under partial and supercavities where the difference is in the extent of the cavity. The partial cavity as the name suggests covers only partially the surface of the body, whereas supercavities engulf the body completely and even extend beyond the dimensions of the body.

- *Vortex cavities* are caused by the low pressure inside vortex cores either in turbulent wakes or inside tip vortices.

Combinations of these formations may also exist on the same body at the same time. See Figure 2.1 for some cavitation structures on a marine propeller.

If the nuclei are subjected to excessively low internal pressures for a sufficient length of time, the destabilized vapor sphere will collapse immediately and violently, as soon as the external pressure increases beyond its threshold. Here the time period required to sustain the nuclei at low internal pressure is long compared to the collapse time, if the exposure time is short the nuclei might oscillate in size instead of growing steadily.

There needs to be a mass transfer to vapor from liquid for the cavity to sustain beyond the inception point. This is maintained by the dissolved gas within the surrounding liquid. Thermal exchange is also a phenomenon that impacts the

(a) Bubble cavity

(b) Tip vortex cavity

(c) Partial sheet cavity

(d) Tip vortex cavity
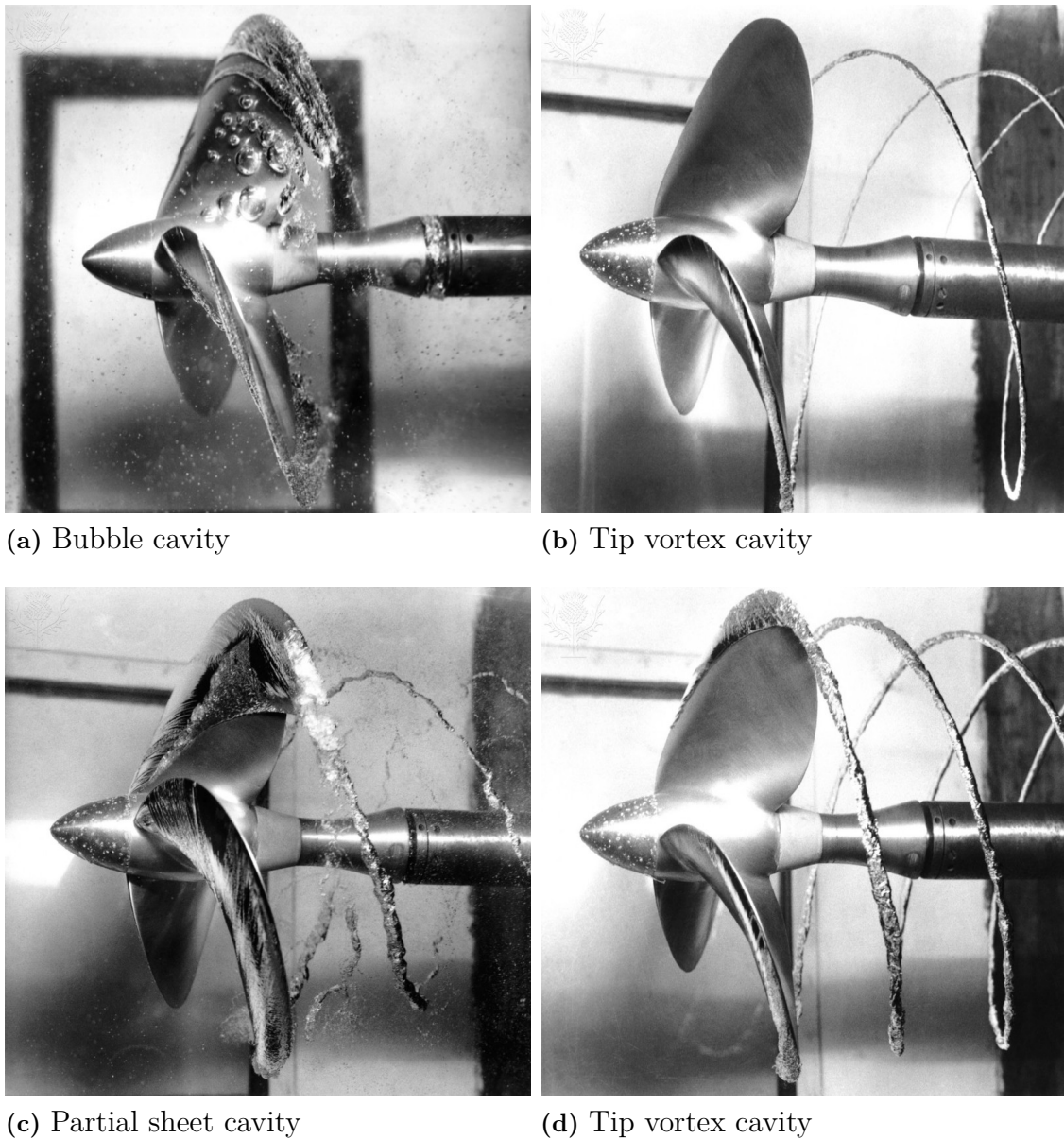
Figure 2.1: Propeller cavitation, courtesy of The National Physical Laboratory.

evolution of cavity from nuclei to inception to collapse as the process is mainly governed through a combination of energy equilibrium equations. This evolution has been aptly described by Franc and Michel (2006, p. 21).

2.2.1 Inception

According to Byrne et al. (2011), the trio of controlling factors behind cavitation inception specific to turbomachinery such as HATTs are understood to be: 1) the tangential speed of the blade, 2) blade orientation and 3) flow velocity. Together with general influencers such as submergence depth/static pressure and fluid properties one will get an image of the state of cavitation in flow.

In general fluid mechanics the cavitation criteria that can be used -regardless whether or not the flow is cavitating- is the non-dimensional cavitation number

$$\sigma = \frac{P_0 - P_v}{\frac{1}{2}\rho V^2} \qquad (2.1)$$

where P_0 is an absolute free stream (reference) pressure, P_v is the vapor saturation pressure at given temperature and V is reference velocity. Note that the free stream pressure is inclusive of atmospheric pressure.

The cavitation number in Equation (2.1) is therefore a property of the general flow and is non-localized. In order to evaluate cavitation inception thus a measure is needed to reflect the local properties of the flow. This comes in the form of a parameter known as the minimum pressure coefficient C_P[1] which is normally negative and defined as

$$C_{P,min} = \frac{P_l - P_0}{\frac{1}{2}\rho V^2} \qquad (2.2)$$

The practical conditions which satisfy the requirement that local pressure (P_l) be equal to the vapor saturation pressure (P_v) gives

$$\sigma = -C_{P,min}. \qquad (2.3)$$

Equation (2.3) is used as the cavitation inception criteria (Franc & Michel, 2006). It is well worth noting that additional parameters such as water impurities and dissolved gas content (e.g. air) play a role in the generation of cavitation nuclei and are disregarded in simulations where a single phase, pure continuum assumption lies behind the definition of the working fluid that is water.

2.2.2 Shedding

As a sheet cavity reaches its maximum chord-wise extent, the macroscopic pressure variations along and over the cavity result in a certain pattern in the velocity field. This velocity pattern known as the *re-entrant jet* which is common in 3D curved foil surfaces (such as that of the NACA 63-8xx series which is used herein) ultimately causes the sheet cavity to detach from the blade surface, this process is known as shedding and is for turbomachinery usually a periodic phenomenon[2].

In CFD the re-entrant jet comes in the form of velocity vectors that approach the axis of symmetry of the sheet cavity from both directions and "swoop" underneath the cavity in the upstream direction thus causing it to detach from the wall surface as demonstrated in Figure 2.2. These are further discussed in the Results chapter.

---

[1]Not to be confused with the power coefficient which uses the same annotation.

[2]It has been argued by Hoekstra and Vaz (2009) that the very concept of the re-entrant jet model is physically inadequate for viscous flow applications as it fails to satisfy mass conservation. It has nonetheless been used for the past three decades as the basis for many successful cavitation dynamics modeling platforms within the potential flow domain.
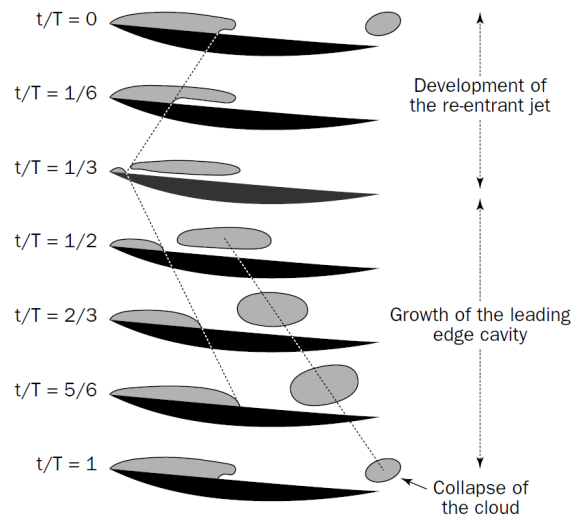
Figure 2.2: Dynamic behavior of partial sheet cavity and the role of the re-entrant jet in cavity shedding (Franc & Michel, 2006).

2.2.3 Collapse

Contrary to the mechanism behind cavitation inception, the collapse of cavities depends on, among other factors the cavity type. A bubble cavity for instance can be terminated by either a collapse under increasing external pressure or a rapid growth that is succeeded by a collapse. It may also sustain an oscillation of consecutive growths and collapses known as a rebound. Alternatively, an unlimited growth may occur that will eventually lead to the transformation of the spherical (bubble) cavity into a greater more complex structure.

The simplification that results in the dynamics described above is only valid as long as contributions from certain parameters such as non-condensible gas content (e.g., air), surface tension and to a lesser extent the effects of viscosity are ignored. When these influencers enter the picture, the governing equations known as *Rayleigh-Plesset* describe a much more complex dynamic behavior (Franc & Michel, 2006).

If it is determined that a marine current turbine is most efficient under cavitating conditions (as is the case with marine propellers) it would become of special interest to investigate the dynamics and life-cycle of the cavities in detail since the erosive nature of cavitation is predominantly due to the collapse mechanism.

2.3 Governing Equations

Flow behavior is frequently described by physical expressions in the form of the Navier-Stokes equations. These equations are the conservation of mass and Newton's second law for viscous fluids assuming the fluid can be treated as a continuum -as opposed to discrete particles- which will be explained below.

2.3.1 Continuity Equation

The balance of mass equation in tensor notation reads (Davidson, 2011)

$$\frac{d\rho}{dt} + \rho\frac{\partial v_i}{\partial x_i} = 0 \tag{2.4}$$

which for incompressible flow (ρ=constant) becomes

$$\frac{\partial v_i}{\partial x_i} = 0. \tag{2.5}$$

2.3.2 Newton's Second Law

The equation for conservation of momentum for a Newtonian viscous fluid is (Davidson, 2011)

$$\sigma_{ij} = -P\delta_{ij} + 2\mu S_{ij} - \frac{2}{3}S_{kk}\delta_{ij}$$
$$\tau_{ij} = 2\mu S_{ij} - \frac{2}{3}\mu S_{kk}\delta_{ij}. \tag{2.6}$$

By entering Equations (2.6) into the viscous stress balance equation

$$\rho\frac{\partial v_i}{\partial t} = \frac{\partial \sigma_{ji}}{\partial x_j} + \rho f_i \tag{2.7}$$

one will get

$$\rho\frac{dv_i}{dt} = -\frac{\partial P}{\partial x_i} + \frac{\partial \tau_{ji}}{\partial x_j} + \rho f_i = -\frac{\partial P}{\partial x_i} + \frac{\partial}{\partial x_j}\left(2\mu S_{ij} - \frac{2}{3}\mu\frac{\partial v_k}{\partial x_k}\delta_{ij}\right) + \rho f_i \tag{2.8}$$

where the last term (ρf_i) represents net volume forces and μ is dynamic viscosity. Conservation of mass for incompressible flow stipulates that the second term in the parentheses be equal to zero, and by taking the constant viscosity outside of the derivative and considering that

$$\frac{\partial}{\partial x_j}(2\mu S_{ij}) = \mu\frac{\partial}{\partial x_j}\left(\frac{\partial v_i}{\partial x_j} + \frac{\partial v_j}{\partial x_i}\right) = \mu\frac{\partial^2 v_i}{\partial x_j \partial x_j} \tag{2.9}$$

the Navier-Stokes equation becomes

$$\rho\frac{dv_i}{dt} = -\frac{\partial P}{\partial x_i} + \mu\frac{\partial^2 v_i}{\partial x_j \partial x_j} + \rho f_i \tag{2.10}$$

which also encompasses the continuity equation. This equation is rightfully also referred to as the transport equation for momentum. These governing equations are only valid if the flow is laminar and single-phase. In the present work however turbulent cavitating flow is the subject of interest and as such should be incorporated into the mathematical models.

2.3.3 Reynolds Averaged Navier-Stokes

Turbulent flow as the name suggests contains fluctuating phenomena. For flow studies one is often interested in the mean values rather than their time histories. A method known as Reynold's decomposition allows one to filter out the fluctuations and obtain the flow variables in their mean form. The instantaneous variables of velocity and pressure for example can be decomposed into (Davidson, 2011)

$$
v_i = \bar{v}_i + v_i' \\
p = \bar{p} + p'
$$

$$(2.11)$$

where the first terms on the right hand sides are the averaged and the second terms are the instantaneous fluctuation value. By time-averaging these equations and using $\bar{v}_i = \bar{\bar{v}}_i + \overline{v_i'} = \bar{v}_i + \overline{v_i'}$ one gets

$$
\overline{v_i'} = 0, \quad \overline{p'} = 0
$$

$$(2.12)$$

thus eliminating the fluctuating terms.

A great reason behind using time-averaging is that numerical methods used for solving the Navier-Stokes equations require fine grids and small timesteps to resolve the many different turbulent scales and capture the unsteadiness of the flow. By using time averaged Navier-Stokes (also called RANS) the computational burden is reduced by allowing coarser grids and relaxed timesteps that only need to correspond to the mean value scales.

It can be shown that the final form of time averaged continuity and Navier-Stokes equations become (Davidson, 2011)

$$
\frac{\partial \bar{v}_i}{\partial x_i} = 0 \\
\rho \frac{\partial \bar{v}_i \bar{v}_j}{\partial x_j} = -\frac{\partial \bar{p}}{\partial x_i} + \frac{\partial}{\partial x_j} \left(\mu \frac{\partial \bar{v}_i}{\partial x_j} - \rho \overline{v_i' v_j'} \right)
$$

$$(2.13)$$

with the assumption that the main flow is steady. The new term $\rho \overline{v_i' v_j'}$ appearing on the right hand side is called the Reynolds stress tensor which represents the correlation between fluctuating velocities and needs to be modeled to close the equation system in (2.13). There are different ways to model this term but in eddy-viscosity models such as those introduced below it is treated as an increase in viscosity, defined as turbulent viscosity μ_t.

Since the turbulence models used herein are widely commercialized eddy-viscosity incompressible RANS models, there will be no need for the underlying modeled equations which can be readily found in contemporary CFD handbooks. For sake of avoiding repetitiveness, the author wishes to cite Versteeg and Malalasekera (2007) as one of available publications for the interested reader. More specific details on the turbulence models' terms, constants and equations are also readily available through the published works cited after their respective titles. The models used thus are k-ω (SST-2003) (Menter et al., 2003) and k-$\sqrt{k}L$ (Menter et al., 2006) herein abbreviated as KSKL which is understood to present superior similarity with experiments as thoroughly described in the reference.

2.3.4 Multiphase Turbulence Modeling

A general transport equation that is valid for turbulent flow is written for the parameter ϕ as

$$\frac{d}{dt}\int \phi dV = \int (\frac{\partial \phi}{\partial t} + \nabla.\phi\bar{u})dV = \int (\frac{D\phi}{Dt} + \phi\nabla.\bar{u})dV, \tag{2.14}$$

it can then take the form of the continuity equation if density of the fluid ρ is used as the transported parameter ϕ thus giving

$$\frac{\partial \rho}{\partial t} + \nabla.\rho\bar{u} = \frac{\partial \rho}{\partial t} + \bar{u}.\nabla\rho + \rho\nabla.\bar{u} = \frac{D\rho}{Dt} + \rho\nabla.\bar{u} = 0 \tag{2.15}$$

which is valid for any control volume. Equation (2.15) simplifies to the continuity equation $\nabla.\bar{u} = 0$ in case of an incompressible fluid as was previously shown, see Equation (2.5).

One way to model multi-phase flows, the VOF method (Hirt & Nichols, 1981), is based on the assumptions that each of the phases is homogeneous and incompressible. For an arbitrary number of phases we have

$$\rho = \sum_{i=1}^{n} \rho_i\alpha_i \quad , \quad \mu = \sum_{i=1}^{n} \mu_i\alpha_i \quad , \quad \sum_{i=1}^{n} \alpha_i = 1 \tag{2.16}$$

where ρ is mass density, μ is viscosity and α_i is the volume fraction of phase i. For the momentum equation, values for mixture density and mixture viscosity as defined by Equation (2.16) need to replace the usual density and viscosity in Equations (2.6). By replacing ϕ with $\rho\bar{u}$ in Equation (2.14) one will get the momentum transport as

$$\frac{\partial \rho\bar{u}}{\partial t} + \nabla.\rho\bar{u}u = \bar{F} \tag{2.17}$$

where $\bar{F}$ includes pressure, viscous and external forces.

The transport equation that governs the volume fractions of the species is defined similar to the momentum equation as

$$\frac{\partial \alpha_i}{\partial t} + \nabla.(\alpha_i\bar{u}) = Q_{\alpha_i} \tag{2.18}$$

with Q_{α_i} as the source term. From the incompressibility of each species it follows that the continuity equation is maintained as $\nabla.\bar{u} = 0$ same as before.

It remains now only to setup a computational premise in which the VOF model can be discretized and solved. Multiphase models including Sauer (Sauer & Schnerr, 2001), Singhal (Singhal et al., 2002), Şenocak (Şenocak, 2002), Kunz (Kunz et al., 2000), Ahuja (Ahuja et al., 2001) and others are available in ReFRESCO. For the present application the *Sauer* cavitation model is selected due to its previous applications with the ReFRESCO solver but also since it is the most physical (or less unphysical) one (Hoekstra & Vaz, 2009) and is now implemented as the solvers default cavitation model. Equation (2.18) is rewritten for the vapor phase as

$$\frac{\partial \alpha_v}{\partial t} + \nabla.(\alpha_v\bar{u}) = Q_v \tag{2.19}$$

using the source term

$$Q_v = \frac{S}{\rho_v} = (4\pi R^2 n_0)(1 - \alpha_v)\sqrt{\frac{2}{3}\frac{|p_v - p|}{\rho_l}} \quad \text{for} \quad p < p_v,$$

$$Q_v = \frac{S}{\rho_v} = -\frac{3\alpha_v}{R}\sqrt{\frac{2}{3}\frac{|p_v - p|}{\rho_l}} \quad \text{for} \quad p \geq p_v \tag{2.20}$$

The original settings proposed by Sauer and Schnerr (2001) are used which are initial nuclei concentration $n_0 = 10^8 \frac{nuclei}{m^3 water}$ and nuclei radii of $R_0 = 30\mu m$. The solver then allows the bubble radius to vary from its initial value through the relation

$$\frac{4}{3}\pi R^3 n_0 = \frac{\alpha_v}{1 - \alpha_v} \tag{2.21}$$

but limits it at all times in the range of $3 \times 10^{-5}m < R < 1.0m$ in order to avoid anomalous radii near the extremes. It has been explained by Hoekstra and Vaz (2009) that the source term in multiphase transport equations (among other effects such as evaporation and condensation) causes regions of the flow with lower mass density to receive greater influence from the momentum exchange.

2.4 Reboud Correction

The *Reboud* correction (Reboud et al., 2003) is an ad hoc method used frequently in the industry when employing RANS simulations for cavitation. Since cavitation contains by nature multiple spatial and temporal flow scales and RANS modelling is an averaging method it can be argued that cavitation is not realistically captured compared with methods solving time varying turbulence, such as any Scale-Resolving-Simulation methods[3]. It is also known, that RANS or URANS methods do damp the intrinsic unsteadiness of cavitating flow, due to the too high eddy-viscosity values at the cavity interface and reattachment zones. One way to deal with this dilemma is to use an explicit correction to the turbulent viscosity based on vapor fraction i.e., the turbulent viscosity is lowered in mixed regions. This method is in fact a modification to the k-ϵ RNG (Yakhot et al., 1992) turbulence model, that enables it to emulate the transient cavitation of a compressible k-ω model which allows density fluctuations (Coutier-Delgosha et al., 2003) as demonstrated for a Venturi-type section with applications further extended to turbomachinery in Reboud et al., (2003).

All k-ϵ models including the standard k-ϵ RNG model which was employed in Yakhot et al., (1992) use the total viscosity μ in the Reynolds equations as defined from the sum of molecular and turbulent viscosity as

$$\mu = \mu_t + \mu_l \tag{2.22}$$

where $\mu_t = \rho C_\mu k^2/\epsilon$ and $C_\mu = 0.085$. The Reboud correction redefines the turbulent viscosity as

---

[3]Such as DES, DDES, SAS, PANS, LES and DNS.

$$\mu_t = f(\rho)C_\mu k^2/\epsilon \tag{2.23}$$

where

$$f(\rho) = \rho_v + (\frac{\rho_v - \rho}{\rho_v - \rho_l})^n(\rho_l - \rho_v) \quad , \quad n \gg 1 \tag{2.24}$$

Arguing that the re-entrant jet is mainly composed of liquid this reduction in eddy-viscosity is understood to be responsible for enabling incompressible RANS equations to capture transient cavitation behavior such as shedding[4] (Coutier-Delgosha et al., 2003). ReFRESCO implements the eddy-viscosity correction in the form of $\mu_{t,corr} = f(\alpha)\mu_t$ where

$$f(\alpha) = \frac{\rho_v + (1 - \alpha)^n(\rho_l - \rho_v)}{\rho_l} \tag{2.25}$$

which is Equation (2.24) re-written for the vapor volume fraction α where n values can vary between 1 and 10 for minimal and maximal eddy-viscosity damping.

Although the Reboud correction to turbulent viscosity has been developed and applied for the k-ϵ RNG formulations, in this thesis it has been used for the KSKL and k-ω (SST-2003) models.

2.5 CFD Tool

The simulations are performed using ReFRESCO v2.1.0, a CFD RANS solver for multiphase viscous flows. It has built-in turbulence and cavitation models (Vaz et al., 2009). The discretization is performed by a finite-volume method using collocated grid arrangement and a variation of the SIMPLE algorithm enforces conservation of mass (Klaij & Vuik, 2013). There is a choice between 1st or 2nd-order implicit backward time discretization schemes. The different equations coupling is restored using a segregated approach i.e., each equation is solved for with regards to a specific variable and then coupling is maintained by the iterative process. An arbitrary number of cell faces as well as hanging nodes are allowed. Modern features including moving, sliding and deforming grids, as well as automatic grid refinement are also available. Aside from RANS, methods such as SAS and DES can be performed and the solver can be used in MPI. It is designed to run on Linux.

The solvers schematic procedure is outlined in Figure 2.3, where the set of equations solved depends on the flow problem at hand. It would be easier to understand this process if one divides them into three iteration loops: the time loop, the outer loop and the inner loop. ReFRESCO segregates the equations which are otherwise coupled and then solves them each with regards to a single variable of interest. All transport equations use the 1st order upwind discretization scheme with the exception of the momentum equation which is discretized using the higher order QUICK

---

[4]The legitimacy of employing the Reboud correction has been questioned due to its *hybrid* nature, where it is effectively transforming the RANS method into something that is not quite physically understood. Like any ad hoc method by definition it resolves a practical issue without providing a universal physical justification.

```
initialization
do (time loop)
   increment t
   do (outer loop)
      solve the momentum equations
      do (inner loop)
         solve linear system of equations
      enddo (inner loop)
      solve the pressure correction equation
      do (inner loop)
         solve linear system of equations
      enddo (inner loop)
      correct velocity field
      solve turbulence model equations
      do (inner loop)
         solve linear system of equations
      enddo (inner loop)
      solve additional transport equations
      do (inner loop)
         solve linear system of equations
      enddo (inner loop)
   enddo (outer loop)
enddo (time loop)
```

Figure 2.3: Solution scheme used by ReFRESCO for time-dependent flow problems (Vaz & Hoekstra, 2006).

scheme, then through the iterative process shown the non-linear character of the equations is restored as well as their coupling. The discretization employs a cell-centered, collocated arrangement, finite volume method (Vaz & Hoekstra, 2006).

In case of unsteady simulations the time discretization is performed by the implicit three time level 2nd order accurate backward scheme.

2.6 Vortex Identification via the Q-Criterion

The existence of vortices and cavitation are closely related as they can both be an indicator for regions of local relative low pressure and high velocity. In turbomachinery they become more relevant because of the rotational nature of the flow. While to a non-mathematician observer it may be quite straight forward to identify a vortex as a circular flow motion, it can be rather difficult for scientists to reach a unanimous verdict on where the vortex structure limits are. To this end flow analysts have been trying to come up with methods that best describe the characteristics of the flow which result in a vortex structure. A very detailed and practical compilation of some of the more advanced methods is available in Holmén (2012).

The present work adopts the *Q-Criterion* method for identification of vortices which is based on the second order velocity gradient tensor. One can decompose

this tensor into a symmetric and an anti-symmetric part as

$$\nabla u = D_{ij} = S_{ij} + \Omega_{ij} \tag{2.26}$$

where $S_{ij} = \frac{1}{2}(\frac{\partial u_i}{\partial x_j} + \frac{\partial u_j}{\partial x_i})$ denotes the rate of strain tensor and $\Omega_{ij} = \frac{1}{2}(\frac{\partial u_i}{\partial x_j} - \frac{\partial u_j}{\partial x_i})$ is the vorticity. A characteristic equation for ∇u is then defined as

$$\lambda^3 + P\lambda^2 + Q\lambda + R = 0 \tag{2.27}$$

where P,Q and R denote the invariants of the velocity gradient tensor. By using the decomposition in Equation (2.26) the Q invariant can be expressed as

$$Q \equiv \frac{1}{2}(u_{i,i}^2 - u_{i,j}u_{j,i}) = -\frac{1}{2}u_{i,j}u_{j,i} = \frac{1}{2}(||\Omega||^2 - ||S||^2) \tag{2.28}$$

where the absolute tensor value $||\mathbf{D}||$ of a tensor $\mathbf{D}$ is defined as $||\mathbf{D}|| = [tr(\mathbf{D}\mathbf{D}^T)]^{1/2}$. The condition of $Q > 0$ is thus used as an incompressible flow vortex identification criterion (Kolář, 2007). By looking at Equation (2.28) one can in plain terms state that the Q-Criterion signifies the prevalence of vorticity over strain-rate. The additional requirement that vortex pressure be lower than ambient pressure makes the Q-Criterion an excellent candidate for cavitation related vortex identification.

2.7 Moving Grids

When resolving the flow around moving objects, it is important to specify the reference frame being used since it will impact the way the Navier-Stokes equations are written.

Depending on the time dependency of the cases, two different ways are used to simulate the rotation of the turbine blades and hub. In case of steady simulations, an Absolute Formulation Method (AFM) is used where the equations are expressed in a body-fixed coordinate and the variables in an earth-fixed reference frame. This method greatly eases the modeling and resource requirements by virtually rotating the computational domain instead of the turbine geometry.

In case of unsteady simulations, both the equations and variables are expressed in an earth-fixed reference frame using the moving grid (MVG) or Arbitrary Lagrangian-Eulerian (ALE) method. Here, the blade and hub geometries rotate in accordance with the respective TSRs and as a result the situation becomes transient i.e., unsteady. Increased computational effort as well as simulation of multiple timesteps is thus required in order to resolve these cases.

3

Case Definition

3.1 The Experiments

One of the cornerstones of the scientific method is the repeatability of the results of experiments conducted by different researchers. More so, is this true in case of numerical methods where validation and verification of results are of high importance.

For this reason the so-called Southampton turbine, a turbine with ample amount of experimental and computational data available is selected. The reference turbine used by Bahaj et al., (2007a), Bahaj and Myers (2003), Bahaj et al., (2007b) and Batten et al., (2008) comprises of three blades and is developed from the NACA 63-8xx foil series as defined in Table 3.1.

Table 3.1: NACA 63-8xx foil series particulars

r/R	Radius (mm)	c/R	Pitch distribution (deg)	t/c (%)
0.2	80	0.125	15	24
0.25	100	0.1203	12.1	22.5
0.3	120	0.1156	9.5	20.7
0.35	140	0.1109	7.6	19.5
0.4	160	0.1063	6.1	18.7
0.45	180	0.1016	4.9	18.1
0.5	200	0.0969	3.9	17.6
0.55	220	0.0922	3.1	17.1
0.6	240	0.0875	2.4	16.6
0.65	260	0.0828	1.9	16.1
0.7	280	0.0781	1.5	15.6
0.75	300	0.0734	1.2	15.1
0.8	320	0.0688	0.9	14.6
0.85	340	0.0641	0.6	14.1
0.9	360	0.0594	0.4	13.6
0.95	380	0.0547	0.2	13.1
1.0	400	0.05	0	12.6

The experimental rig consists of the three-bladed rotor fixated on a yaw-controlled shaft which drives the generator above the vertical support tube. The setup can be seen in Figure 3.1, with a view from inside the cavitation tunnel of the assembled model in Figure 3.2.
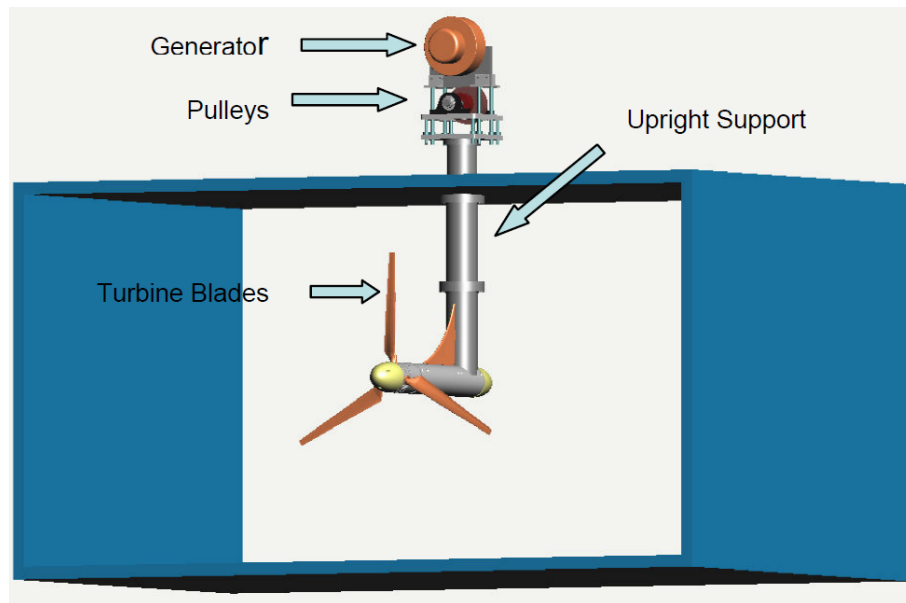
Figure 3.1: Computer model of the experimental rig in the cavitation tunnel. Photograph courtesy of Bahaj, Molland, et al. (2007), University of Southampton.
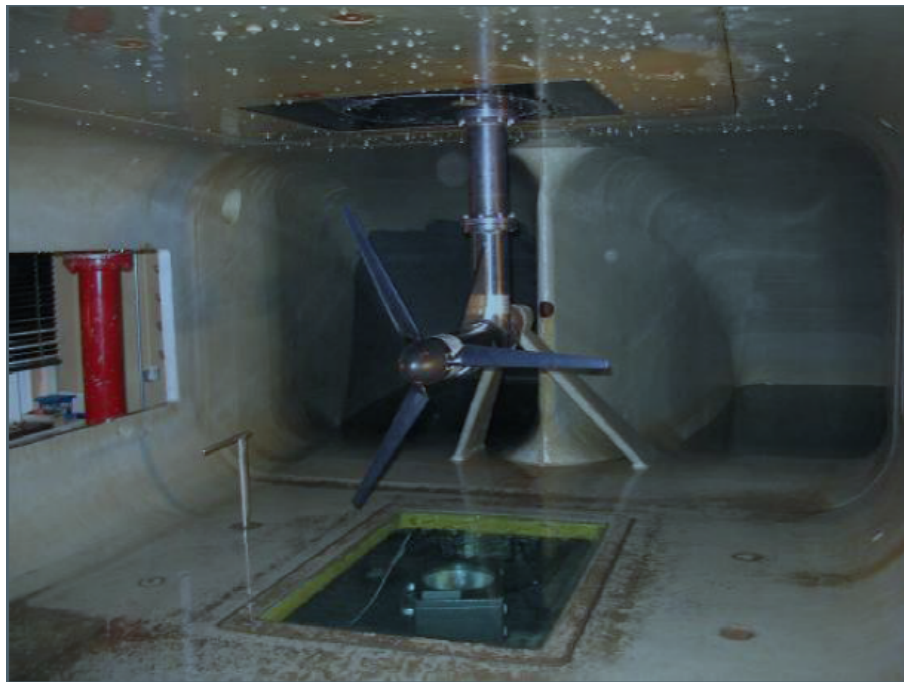
Figure 3.2: Inside the cavitation tunnel looking downstream. Photograph courtesy of Bahaj, Molland, et al. (2007), University of Southampton.

Several operating conditions have been used in the experiments and a broad range of data exists as a result. Two of these operating conditions have been selected in relevance to the present thesis. These are the TSR diagram studies (case A) and the cavitation simulations (case B). The results are expressed in terms of the non-dimensionalized parameters C_P and C_T against TSR in Figure 3.3.
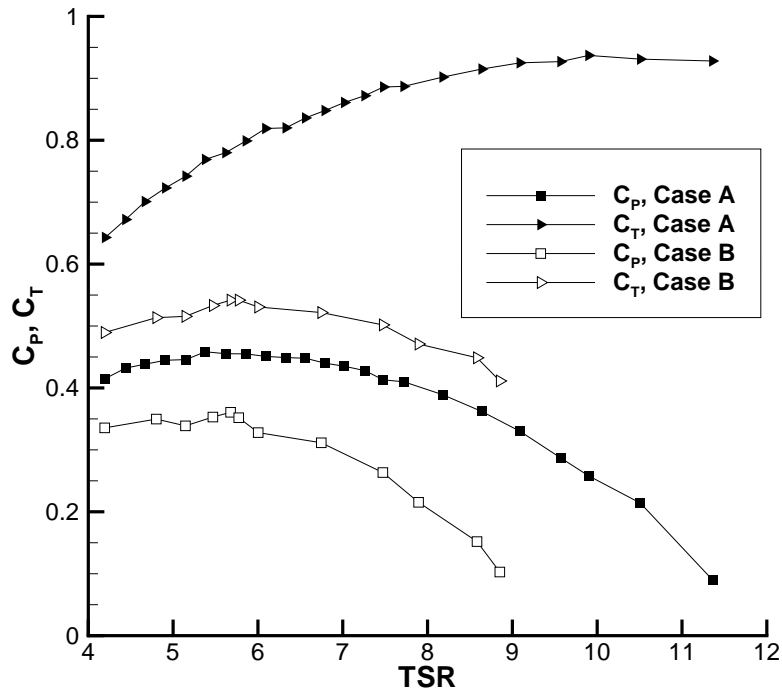
Figure 3.3: Experimental results for two operating conditions, reconstructed after Bahaj, Molland, et al. (2007).

3.2 Numerical Setup

Initially the same *HexPress* grid as in Otto et al., (2012) was used which is an unstructured grid with hanging nodes. The grid was too big and concessions were made to the trailing edge geometry which intrinsically delivered less accurate results. The fact that it was unstructured practically inhibited proper verification studies. As easy as it is to make, it is indeed designed using older techniques and has been discarded.

The newer grids used herein are generated using *GridPro* and have substantially reduced file sizes. Since these are overlapping grids, this leads to the presence of a mesh interface. Credit goes to Lampe (2015) for generating these grids as well as performing wetted flow simulations as was mentioned in the literature survey. Table 3.2 lists cell counts for used grids and Figures 3.4 and 3.5 show the blades meshes. The grids with the straightened blade root are used for *Case A* simulations and the grid with designation 0.64* (G3*) is used for *Case B*. There have been no simplifications applied to the trailing-edge, and the series of geometrically similar grids now facilitate the application of verification procedures. Although they enable the generation of coarser grids these are relatively more cumbersome to make compared with the HexPress mesh.

In order to avoid increased computational burden, for the the non-cavitating cases used to obtain the TSR diagrams, the geometry of the blade roots are modified

Table 3.2: Grid summary

Grid Name	Grid Designation	Interior Cells	Blade Root
G1	0.4096	3,069,888	Straightened
G2	0.512	7,464,720	Straightened
G3	0.64	15,720,024	Straightened
G4	0.8	29,102,472	Straightened
G3*	0.64*	8,390,592	Cylindrical

from that of the model used in the cavitation tunnel experiments. The connection between the blade root and the hub has been straightened from its original cylindrical profile to one resembling a continuation of the blade section, as seen in Figure 3.7b. This is done to prevent an unsteady wake which would impose larger computational effort needed to accommodate for solving the added turbulence. The uncertainty that arises from this modification has been previously demonstrated in Otto et al., (2012). For cavitation simulation series however, a realistic blade geometry is used because of the already resource-intensive nature of the computations, see Figure 3.7a.

Attention is drawn to the fact that two different blade pitch geometries are used in this thesis, expressed by the *Hub Pitch Angle*. The non-cavitating TSR diagram calculations (case A) use a blade geometry with a set angle of 5 degrees which translates to 20 degrees hub pitch angle. The cavitating calculations (case B) uses blade geometry with 10 degrees set angle, resulting in hub pitch angle of 25 degrees. These two cases are also different in the way that their respective reference velocities are defined; for the TSR diagrams the point of interest is at $r/R = 0.7$ where it is believed to generate maximum lift, for the cavitation case however the blade tip is of greater importance since most of the cavity is located near the tip. This distinction is applied through the definition of the *localized resultant velocity*:

$$V_{res} = \sqrt{U_T^2 + (\omega r)^2} \tag{3.1}$$

where local radius r is set to $0.7R$ for TSR diagram cases and R for cavitation studies[1]. Another differentiating factor is the tunnel inflow velocity U_T which is set to $1.73[m/s]$ for case A and $1.4[m/s]$ for case B. The difference is due to the different benchmark conditions that were used to validate each of these series of simulations. Case particulars have been summarized in Table 3.3 indicating that for case A only wetted flow simulations for multiple TSRs have been performed including a grid refinement study, and for case B cavitating flow simulations for a single TSR are performed without a grid refinement analysis.

3.3 Computational Domain

The Inflow BC is placed on a distance equal to 8 rotor diameters upstream and the Outflow BC is 8 diameters downstream of the rotor plane. The external cylindrical

---

[1]This velocity is used for the cavitation inception indicator in Equation (2.2).

(a) G1   **(b)** G2   **(c)** G3   **(d)** G4
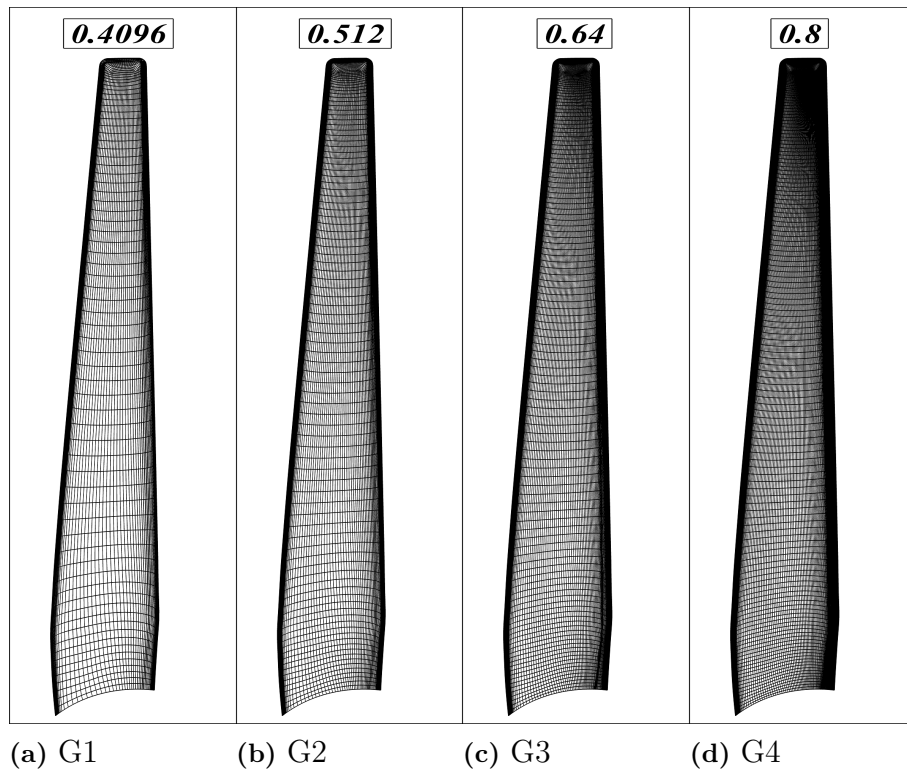
Figure 3.4: Straightened blade-hub connection geometry, pressure side.

(a) G1   **(b)** G2   **(c)** G3   **(d)** G4
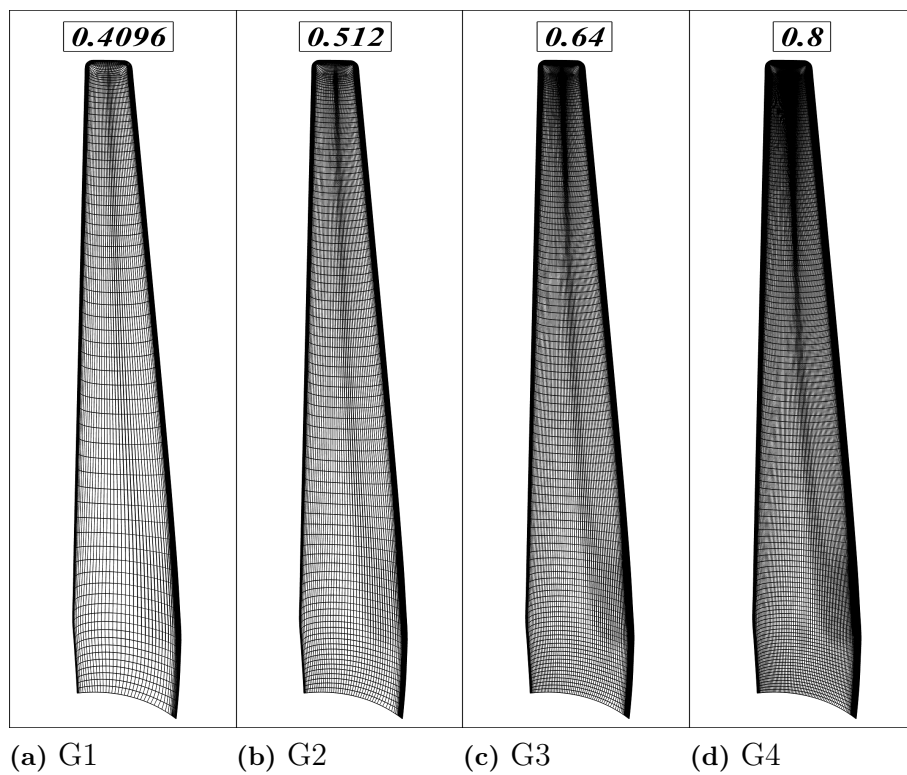
Figure 3.5: Straightened blade-hub connection geometry, suction side.

(a) Pressure side   **(b)** Suction side
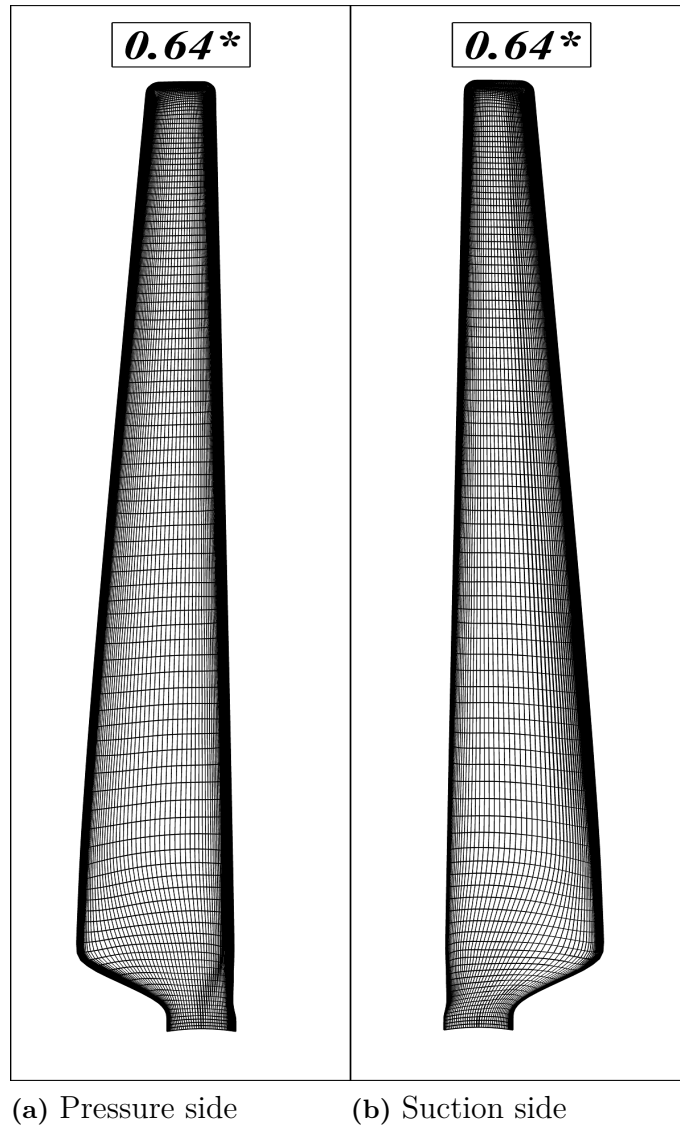
Figure 3.6: Cylindrical blade-hub connection geometry for grid G3*.

Table 3.3: Simulation setup summary

Case	Steady Wetted Flow	Unsteady Wetted Flow	Cavitating Flow	U_T [m/s]	Hub Pitch Angle	V_{res} Radius	Blade Root Geometry
A	✓	✓	-	1.73	20°	$0.7R$	Straight
B	✓	✓	✓	1.4	25°	R	Cylindrical

Pressure BC has a radius 8 times the rotor diameter. This large domain (Figure 3.8) is selected in order to eliminate the boundary effects on the flow near the turbine, however it is believed that this simplification will introduce a level of uncertainty which has been previously addressed and quantified by Otto et al., (2012). The no-slip wall BC is used for blades and the hub. Zero yaw is used in all simulations.
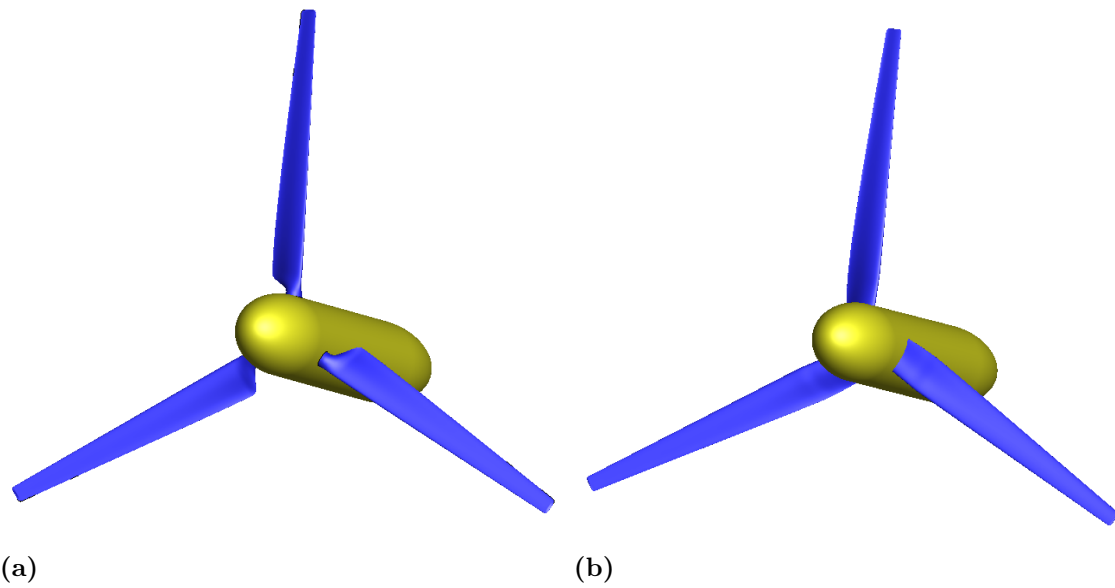
Figure 3.7: Blade root geometries used in (a) cavitating case with hub pitch angle 25°, (b) TSR diagram cases with hub pitch angle 20°.
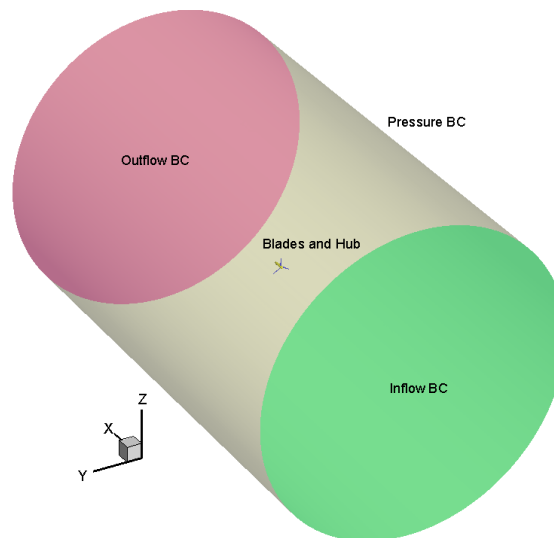
Figure 3.8: Computational domain and boundary conditions.

An Inflow BC assumes the three velocity components to be given by a Dirichlet condition, while the pressure is extrapolated to the boundary from the interior. On Outflow boundaries the convective flux is evaluated using zeroth order extrapolation, implying that the cell center values substitute face values. The pressure or the pressure gradient normal to the boundary thus needs to be known since in an Outflow BC all quantities (including pressure) are calculated by considering a Neumann BC where the normal gradients are equal to zero (Vaz & Hoekstra, 2006).

3.4 Strategy

The work is conducted in two separate but similar parts: TSR diagram studies (case A) and cavitation studies (case B). A visual breakdown of the procedure is displayed in Figure 3.9 where the first two stage are common for both cases A and B, but the final stage (multiphase simulations) is only performed for case B.

Since this research is based on one experimental and two Computational Fluid Dynamics (CFD) studies, alterations to the configurations used in previous simulations must be checked not to disturb the integrity of the results. For this purpose every new result shall be confirmed against an appropriate benchmark i.e., the experimental results for that specific set of conditions. After establishing the working mesh, working turbulence model and cavitation tunnel configuration (inflow velocity, turbine RPM, reference pressure) the following general procedure is performed:

1. A steady state TSR study using the AFM equations is performed.

2. The solution of the AFM is used to initiate an unsteady RANS wetted flow TSR study.

3. The solution of the converged URANS simulation is resumed for the TSR of interest with the cavitation model activated. The resulting flow field is the final solution that the investigations will be based on. The flow is analyzed with regards to vapor content, velocities (to identify jet-streams and vortices), pressure distribution, and thrust and power coefficients.[2]

At each stage the overall results are verified against the benchmark cases by looking at the C_T and C_P coefficients. See Section 1.3 for these definitions.

[2]Refer to Table 3.3 for different setup definitions.
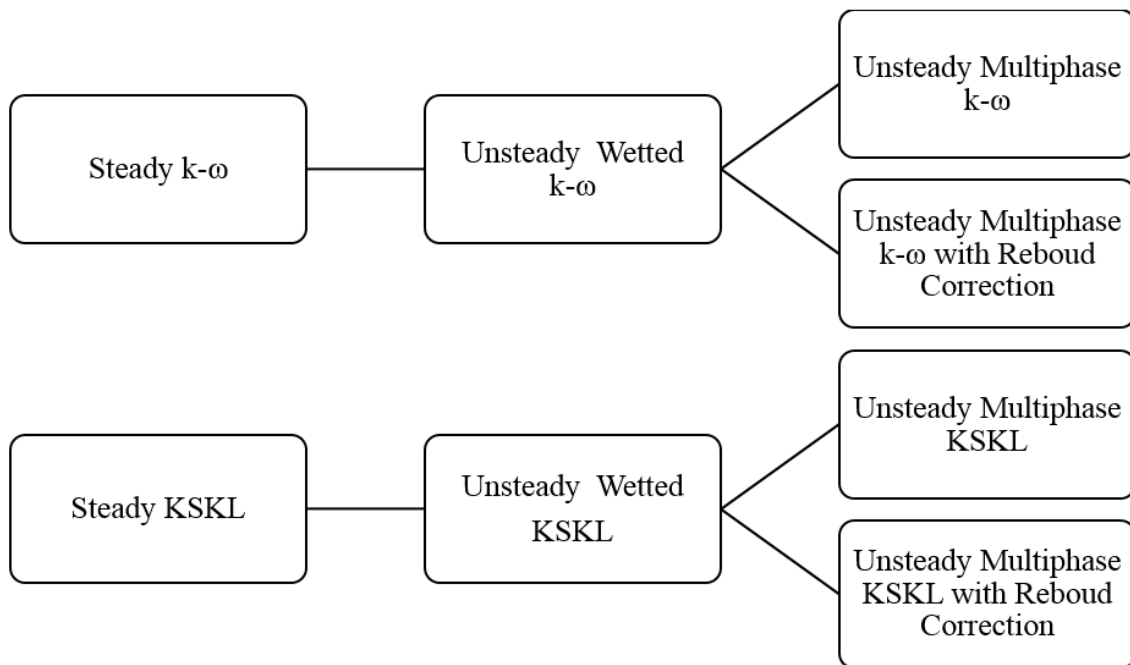
Figure 3.9: General simulation work-flow.

4
Verification Study

An inherent property of turbulence modeling is that the physical problem is not directly solved, instead it is modeled. It is then inferred that errors exist within the obtained results of such a calculation. These errors and uncertainties are twofold; on one hand there is a question of how accurately the modeled problem represents the physical problem, this is the subject of *validation* procedures. On the other hand the solutions to the equations must be verified to have been solved using the correct numerical methods, which leads to *verification*.

As far as validation is concerned the modeling error is only as good as the certainty of the benchmark results (in this case the cavitation tunnel experiments). For verification however a set of standard procedures can be performed on the obtained results in order to measure the uncertainties associated with the numerical methods in use. This is the subject of the current chapter.

Before a case-specific verification study can be performed on the task at hand, the CFD code needs to be verified through a process that is naturally called *code verification*. For commercial packages such as ReFRESCO, code verification is usually performed well ahead of the release of the software and for various test cases. In addition, later studies have engaged the issue of code verification for ReFRESCO such as that of Vaz et al., (2009), Toxopeus and Vaz (2009) and Rijpkema and Vaz (2011). The subject is therefore not touched upon within the present work since the software is believed to have been adequately verified.

A verification study for application of ReFRESCO on the Southampton HATT was previously carried out in Otto et al., (2012) with satisfactory results. The grid refinement study is however performed once more here in the first simulation stage (steady cases) in order to optimize run-times and resource allocation as well as to determine the numerical uncertainty of the CFD results. This is of course facilitated by the structured grids which permit a systematic cell size reduction, crucial for assessment of the discretization error; see subsection 4.1.1 below.

4.1   Uncertainty Estimation

As stated by Eça et al., (2010b) the lack of knowledge of numerical uncertainties for a calculation could lead to fallacious conclusions.

The numerical uncertainties as defined by Eça et al., (2010a) refer to the interval that contains the exact solution to the problem expressed with a certain degree of confidence. The aim is to maintain this interval below 5% of the solved value

$$\phi_i - U_\phi \ll \phi_{exact} \ll \phi_i + U_\phi \tag{4.1}$$

where U_ϕ is the numerical uncertainty of the solution ϕ_i for an unknown exact solution ϕ_{exact}.

It is generally accepted that the uncertainties comprise of three main components which are the round-off error, the iterative error and the discretization error. Round-off errors are easiest to alleviate since using a precise enough number of digits in the calculations reduces this to acceptable levels. By using double digit (10^{-16}) precision this error can be considered negligible. The iterative error is addressed in Section 4.1.2 and is not attained in all TSRs for all grid densities, therefore safety factors must be introduced as will be explained shortly. Consequently the uncertainty will be dominated by discretization errors, which are a result of a) the non-linearity of the equations that are solved in CFD, and b) the approximation that finite-volumes represent a fluid continuum and algebraic equations represent PDEs.

4.1.1 Discretization Uncertainty

The use of the finite volume method in solving RANS equations introduces errors that are caused by the size of the cells. In principle by using an infinite amount of cells, thus reducing their size to zero one must obtain results with very little discretization error. In practice, not only is this not possible due to computational limitations it is also not always the case that a solely larger cell count necessarily improves certainty. A procedure must then be performed to evaluate the amount of this uncertainty to accompany the results.

The Richardson Extrapolation (RE) is a frequently used method for estimating the discretization error ϵ as

$$\epsilon \simeq \delta_{RE} = \frac{\phi_i - \phi_1}{\left(\frac{h_i}{h_1}\right)^p - 1} \tag{4.2}$$

with subscript $_1$ referring to finest grid properties. It is stated by Eça et al., (2010b) that due to the sensitivity of the observed order of accuracy for a grid refinement study the error estimator in Equation (4.2) alone is not a reliable indicator, and as a result three separate error estimators are defined which will be used based on the value of p. Although within the monotonic convergence criteria of $p > 0$, when the achieved curve fits are outside the "reasonable" range of $0.95 \leqslant p \leqslant 2.05$, the following definitions are used as error estimators:

$$\begin{aligned}
U_\phi &= \min(1.25\delta_{RE} + U_s, 3\delta_{RE}^{12} + U_s^{12}) \quad \text{for} \quad p \leq 0.95 \\
U_\phi &= \max(1.25\delta_{RE} + U_s, 3\delta_{RE}^{02} + U_s^{02}) \quad \text{for} \quad p \geq 2.05
\end{aligned} \tag{4.3}$$

with U_s, U_s^{02} and U_s^{12} being the standard deviations of the least squares fits. The additional error estimators used above are defined as $\delta_{RE}^{02} = \phi_i - \phi_0 = \alpha_{01}h^2$ and $\delta_{RE}^{12} = \phi_i - \phi_0 = \alpha_{11}h + \alpha_{12}h^2$ determined in the least squares sense.

In order to perform the verification procedures it is required that the results are converged to the asymptotic range. Turbulent flow, especially in the presence of cavitation is known to not satisfy this requirement easily when modeled using eddy-viscosity RANS models (Eça et al., 2010a). This should be considered and is taken into account by use of safety factors for expressing the numerical uncertainty

Table 4.1: Discretization uncertainties for G3 grid calculations using k-ω (SST-2003), safety factor of 3 applied

TSR	4	5	6	7	8
$U_{C_P}[\%]$	7.9	5.6	3.6	1.8	0.6
$U_{C_T}[\%]$	20.4	1.2	0.7	1.7	2.0

as $U_\phi = F_s|\epsilon|$. The safety factor is dependent on proximity of the observed order of accuracy to the formal order of accuracy and ranges between 1.25 and 3. It is recommended to select safety factor of 3 in cases where it is known that the grid is too coarse to yield asymptotic range results even if the observed order of accuracy is satisfactory.

When monotonic convergence is not observed (for instance oscillatory convergence), the use of safety factor 3 is warranted and since RE no longer applies, an alternative error estimator (with linear accuracy) is defined. Equation (4.2) should then be modified to

$$\epsilon = \frac{\delta_\phi}{\left(\frac{h_i}{h_1}\right) - 1} \tag{4.4}$$

where δ_ϕ is the range of data i.e., the range between the two most different values.

Table 4.1 lists the discretization uncertainty values for C_P calculated from Equation (4.2) and for C_T from Equation (4.4). These procedures have been performed for the k-ω (SST-2003) turbulence model with the G3 grid used as the target of the uncertainty analysis. Although verification here is applied only to the steady simulations, a similar approach can be performed by taking into account not just space but also time refinement to be applied to the unsteady cases. In principle, uncertainty is case-dependent therefore the procedures have been performed independently for each TSR value. Important to mention is that the extrapolated value of the flow parameter itself can not be used as *result*, since its sole purpose is to estimate the *error* of the flow parameter (Eça et al., 2010a).

4.1.2 Iterative Convergence

The system of governing equations of flow is nonlinear, and RANS solvers such as ReFRESCO deal with this nonlinearity through an iterative process where with each round of iteration the solution error becomes smaller and the solved parameters approach an acceptable range of their actual (mathematically solvable) values.

Following the practice of Make and Vaz (2015) the iteration error can be estimated using values of any integral quantity ϕ (in our case C_P and C_T) from the last 200 outerloops as

$$U_i = \max\left(\frac{|\phi_i - \phi_{end}|}{|\phi_{end}|}\right) \tag{4.5}$$

where ϕ_i is the integral quantity at iteration i. This error is deemed negligible as long as it is two orders of magnitude smaller than the discretization error. Table 4.2 displays the attained values which are mostly a fraction of a percent except for the lowest TSR. The error is thus considered as negligible; however the behavior with regards to residuals is further discussed below.

(a) TSR4

(b) TSR5

(c) TSR6

(d) TSR7

(e) TSR8
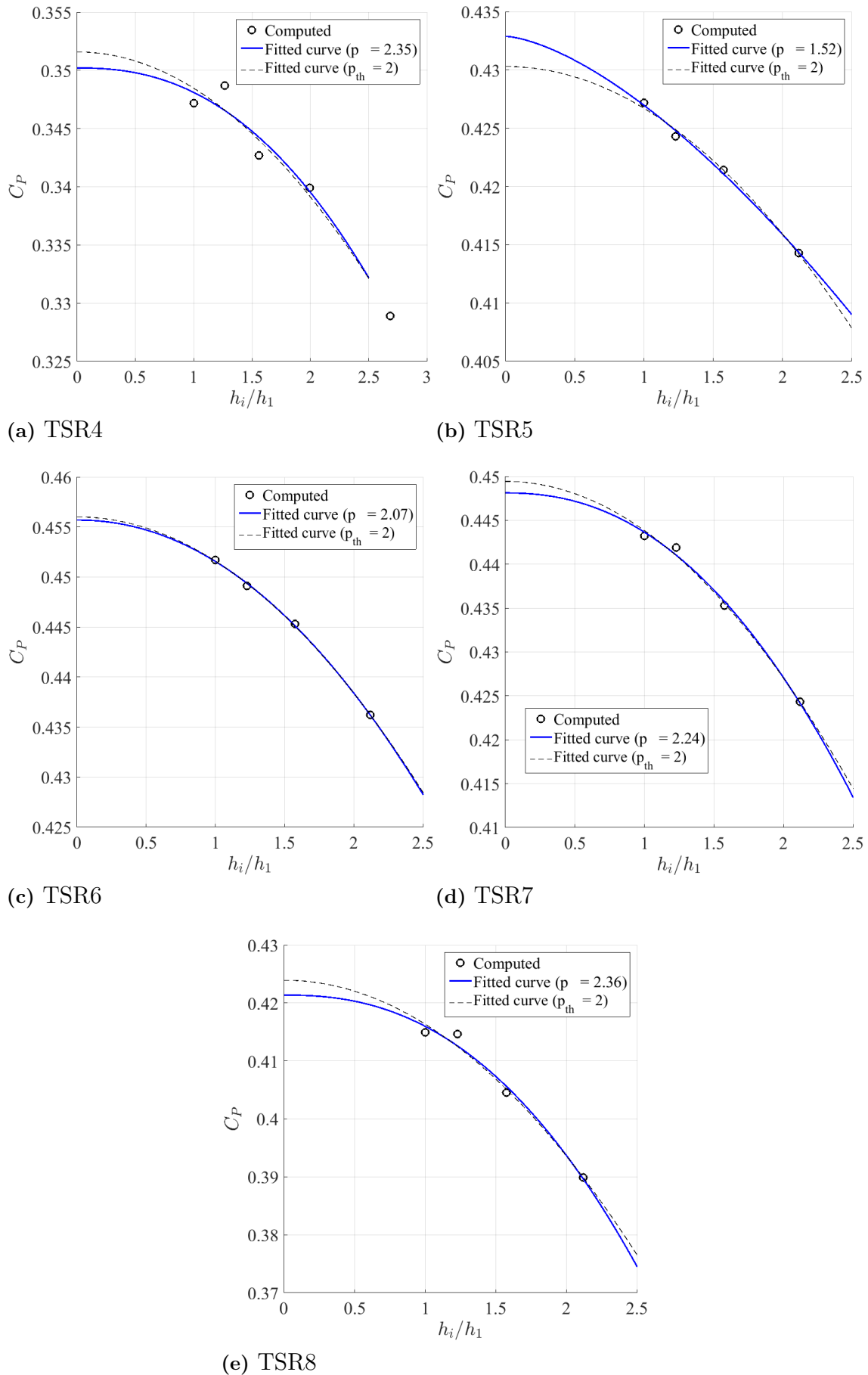
Figure 4.1: Least square fits for C_P values.

Table 4.2: Iterative uncertainties for G3 grid calculations using k-ω (SST-2003)

TSR	4	5	6	7	8
$U_{C_P}[\%]$	0.69	0.02	0.05	0.05	0.09
$U_{C_T}[\%]$	1.16	0.01	0.03	0.02	0.04
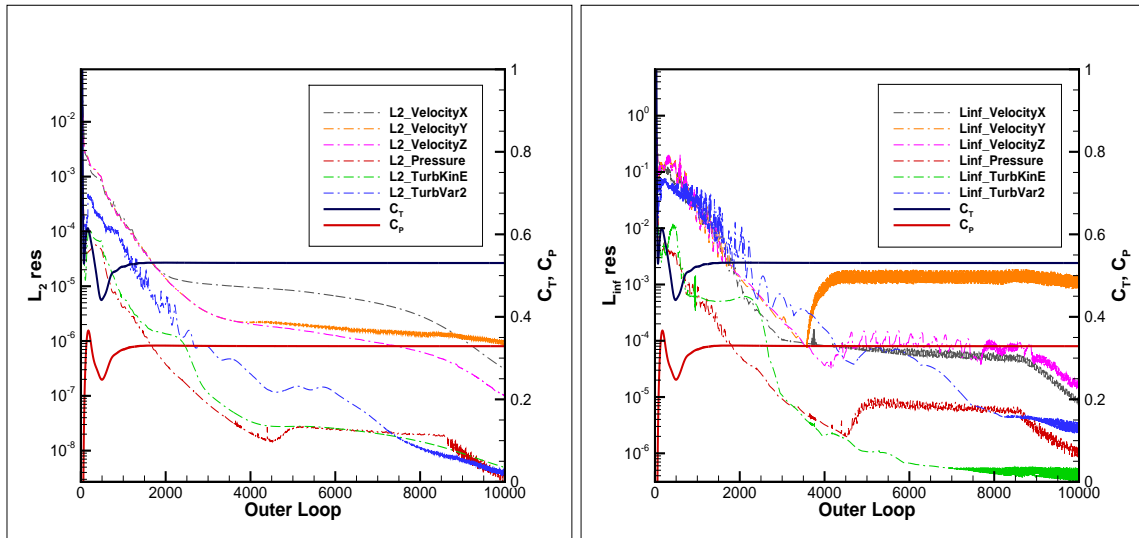
(a) L_2 Residual Norms

**(b)** L_∞ Residual Norms

Figure 4.2: Residual norms decreasing for steady calculations at TSR=4, G1 grid.

The *residual* is a mathematical term defined for each equation which represents the error $F(x^*) - b$ as obtained by inserting the approximate solution x^* into the equation $F(X) = b$. Consequently the residual for any equation has the same dimensions as that equation.

ReFRESCO normalizes the residuals in the form of L_2 and L_∞ norms. The residual norms that were earlier obtained by Lampe (2015) using the same grids as herein proved to be unsatisfactory since they stagnated at high levels close to 1. In the present work the stagnation is still observed for most TSRs and most mesh densities, except now at one order lower values (close to 0.1). In some cases such as that of the Fine grid at TSR=8, or the Coarse grid at TSR=4,8 the residual norms seem to be dropping continuously which presents a possibility for good iterative convergence given enough simulation time. The median TSR value of 6 always exhibits highly oscillating behavior and its average value stagnates. The convergence behavior of the calculations is thus highly case dependent as Figures 4.2 and 4.3 display residual norms for two of the grid densities that were used in the grid refinement study as explained in Section 4.1.1.

Since convergence behavior is not satisfactory, the location of the highest residuals becomes of interest. Maximum velocity residuals are shown in non-normalized form for the two cases of wetted and cavitating flow in Figure 4.4. The wetted flow appears to be unable to converge near to the hub and trailing edge vortices while for cavitating flow the maximum residuals exist mainly at the cavity closure line (See Figure 5.20 for extent of cavity). One should not ignore the effect of re-
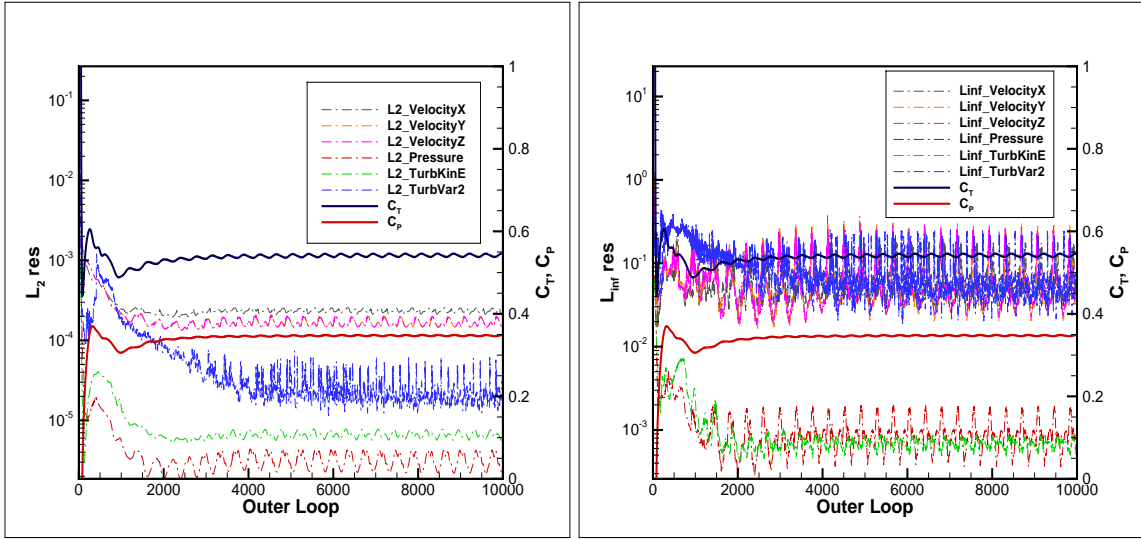
(a) L_2 Residual Norms   **(b)** L_∞ Residual Norms

Figure 4.3: Residual norms stagnating for steady calculations at TSR=4, G4 grid.

fined timesteps with the cavitating simulations which has clearly contributed in the reduction of residuals.

4.2   Considerations on EFD Data

The experimental results do not include an uncertainty analysis and are therefore unfit to be used in a proper validation procedure[1] due to the lack of error margins. "Graphical comparison" of the obtained results in the form of the thrust C_T and power C_P coefficients is therefore used as the only measure of evaluating the computational results resemblance to real world results.

The modified blade to hub connection geometry is assumed as in Otto et al., (2012) to have influence on the uncertainty of the thrust and power coefficient measurements. These were previously evaluated for the single TSR of 5.15 by stating the difference between C_P and C_T predictions for cylindrical and straightened blade root geometry. The resultant uncertainties were found to be 0.5% for C_P and 2.6% for C_T values where the same uncertainty was assumed to be valid for all TSRs. Naturally these values could not be used herein due to the different grids in use and a fresh validation is in order. However as mentioned, in the absence of experimental measurements uncertainty values a validation procedure is postponed.

---

[1]Such as that of ASME V&V 20 (Zou & Larsson, 2014) for instance.

(a)

(b)

(c)
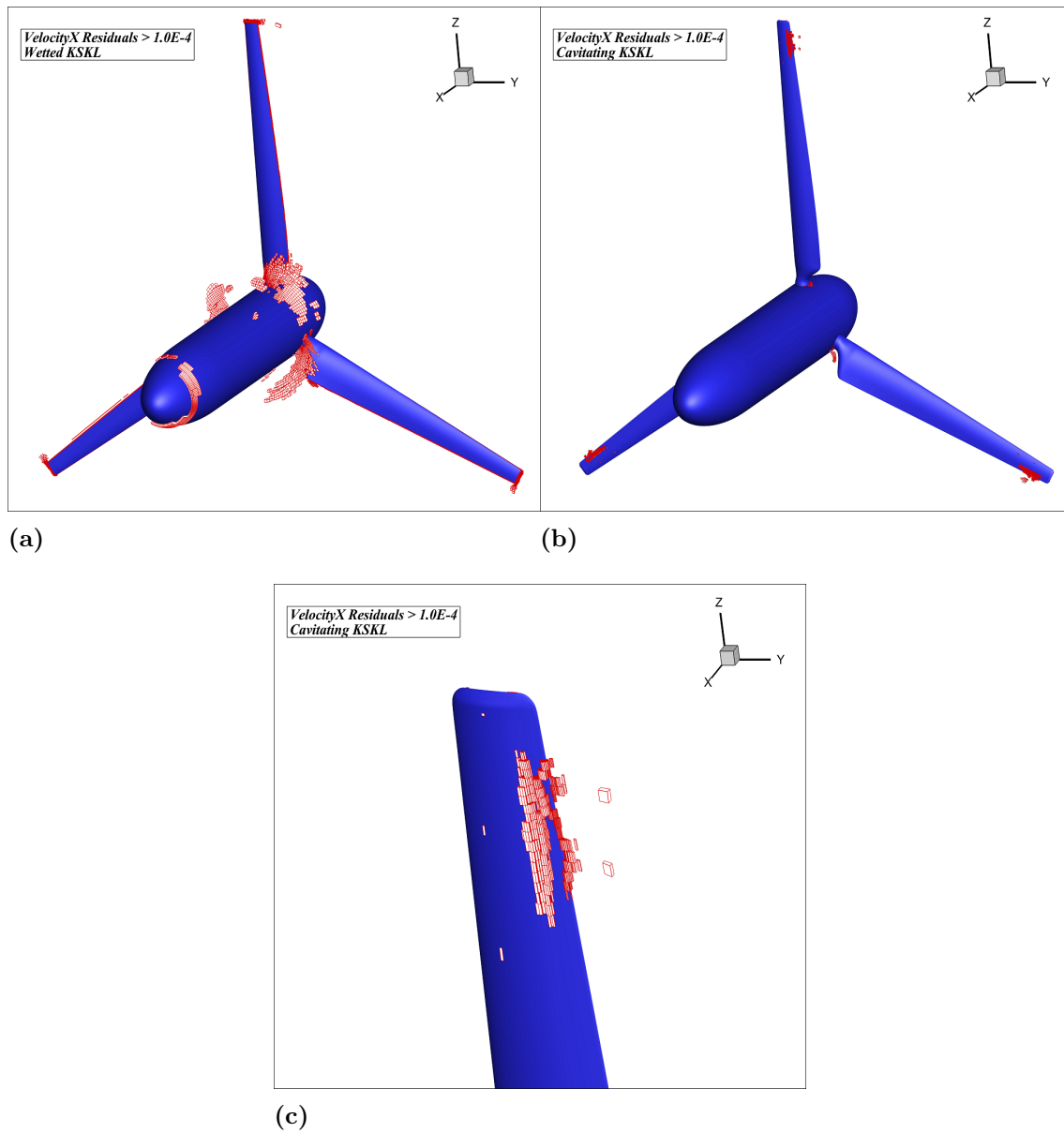
Figure 4.4: Position of cells with maximum VelocityX residuals: (a) unsteady wetted flow, (b) unsteady cavitating flow and (c) near cavity closure line.

5

Results

5.1 Steady Wetted Flow Analysis

The resulting thrust and power coefficients for TSRs 4 through 8 on medium density grid are displayed in Figure 5.1. Disagreement with experimental values is observed to be greatest in the lower TSRs. These are indeed operating conditions with more flow separation observed along the span of the blades and could indicate that the simulation needs to improve in capturing transitional flow.
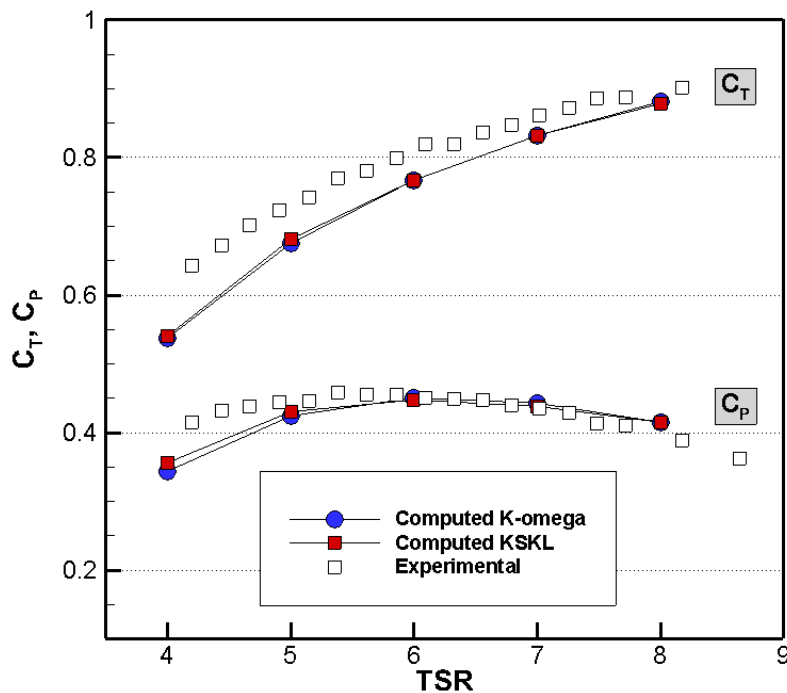
Figure 5.1: Steady computation thrust (C_T) and power (C_P) coefficients against experiments for $U_T = 1.73[m/s]$ and 20° Hub Pitch Angle.

The error bars correspond to the numerical uncertainties as calculated in Chapter 4. Grid convergence uncertainty for medium grid dominated the verification analysis and the results have therefore been used for both turbulence models, although the verification study was performed only for k-ω (SST-2003). Compared with thrust coefficients, the smaller discrepancy of the power coefficient with experiments suggests that the anomalous force predictions may be located nearer to the blade root thus having smaller contribution to the torque values -which are then

used for calculating the power coefficient. This is investigated by observing the pressure distribution and the limiting streamlines on the pressure and suction sides for different TSRs using the k-ω model in Figures 5.2 and 5.3. The pressure distribution is displayed through the non-dimensionalized pressure coefficient C_{pn} here defined as

$$C_{pn} = \frac{P - P_\infty}{\frac{1}{2}\rho(nD)^2} \tag{5.1}$$

where $P[Pa]$ is local pressure, $P_\infty[Pa]$ is tunnel inflow pressure which is set to zero for reference, $n[1/s]$ is revolutions per second and $D[m]$ is rotor diameter. Lower values of the pressure coefficients at the blade tip for all TSRs and on the leading edge of the pressure side at TSR=8 indicate the possibility of cavitation in these regions and is further investigated below in the cavitating flow analysis. The leading edge pressure drop at TSR=8 can be further recognized as one cause behind the power coefficient decrease in the TSR diagrams.

Due to the fact that no slip boundary conditions are applied to the blade surfaces it is not possible to visualize streamlines immediately on the blades as it will display the rotational speed of the blade itself. Instead by plotting the shear stress on the blades in vectors one can visualize what is an indication of the limiting streamlines. The pattern of decreased flow separation regions is clearly visible as TSR increases.

5.2 Unsteady Wetted Flow Analysis

By using the solutions of the steady cases for field initiation, the blade and hub geometries are then rotated using the MVG method instead of AFM. Flow is solved at 3 degree intervals due to best-practice guidelines for propellers in ReFRESCO which results in the force and power predictions seen in Figure 5.4.

Compared with the steady results, an improvement in terms of agreement with the experimental results can be seen. This is indeed expected since the physical case in question is an unsteady one which demands a transient numerical setup in order to reproduce the flow in its entirety. For this reason the pressure distribution and the flow regime is visualized in Figures 5.5 and 5.6 for the pressure and suction side of the blade for 5 TSRs after one revolution. Interestingly for the lower TSRs where large disagreements with experimental data had been observed in steady calculations, the pressure distribution is now higher which explains the improved thrust and power predictions. This indicates that in order to resolve the flow conditions in which larger flow separation across the span of the blade exists, simulation of the flow in transient mode yields more realistic results. It is an interesting finding in that the steady simulations performed previously in Otto et al., (2012) for instance had already attained reasonable results without the use of time discretization.

Additionally in the lower TSRs the KSKL model appears to deliver better results which is in fact attributed to longer running times. It has been observed from the steady simulations and another unsteady case (not presented in this report), that the two turbulence models yield close force and power predictions under similar running times.

Thrust and power coefficient variations with time are shown for TSR=7,8 in Figures 5.7 and 5.8 where 120 timesteps equal one revolution and each timestep

(a) TSR4 **(b)** TSR5 **(c)** TSR6 **(d)** TSR7 **(e)** TSR8
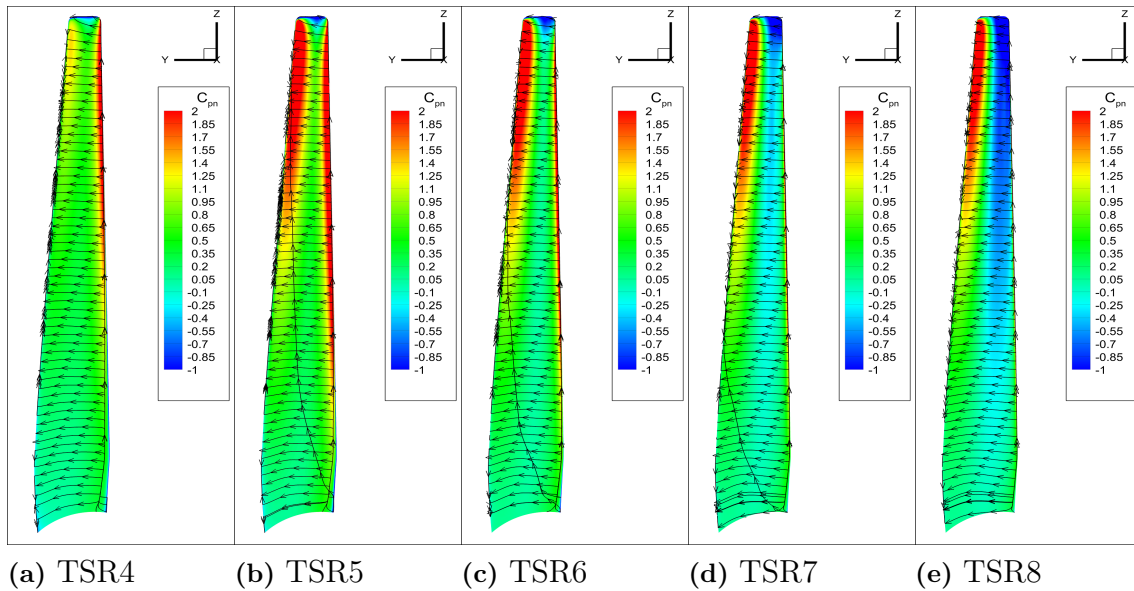
Figure 5.2: Pressure distribution and limiting streamlines for steady calculations, pressure side. $U_T = 1.73[m/s]$ and 20° Hub Pitch Angle using k-ω (SST-2003).

**(a)** TSR4 **(b)** TSR5 **(c)** TSR6 **(d)** TSR7 **(e)** TSR8
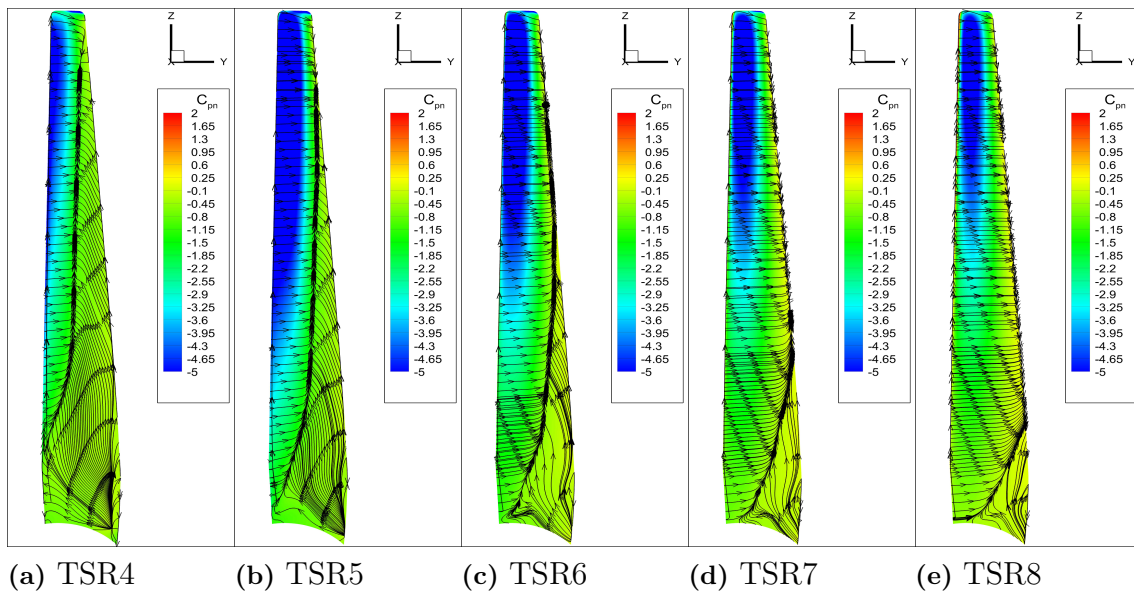
Figure 5.3: Pressure distribution and limiting streamlines for steady calculations, suction side. $U_T = 1.73[m/s]$ and 20° Hub Pitch Angle using k-ω (SST-2003).
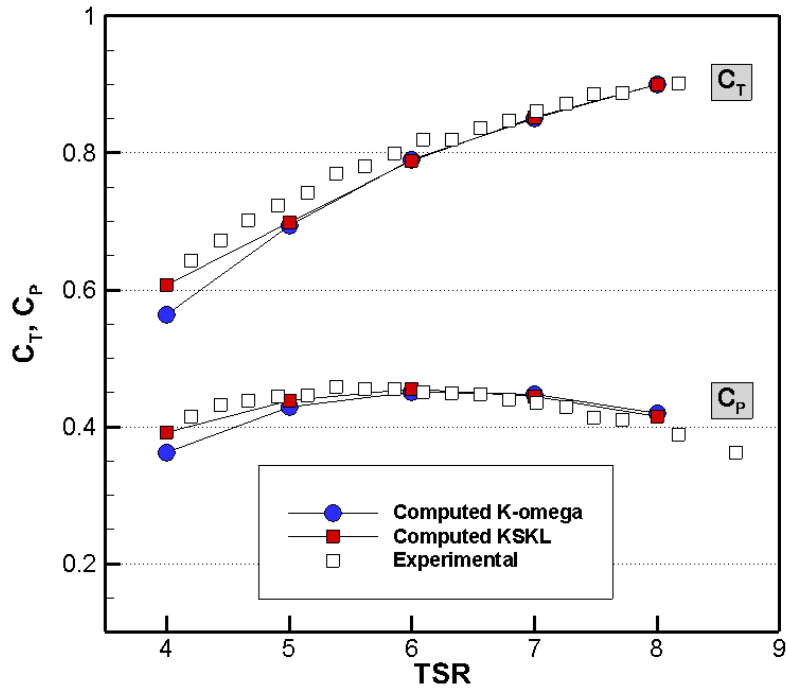
Figure 5.4: Unsteady computation thrust (C_T) and power (C_P) coefficients against experiments for $U_T = 1.73[m/s]$ and 20° Hub Pitch Angle.

represents 100 outer loop iterations. It is observed that the stabilized values are obtained at one revolution which is more or less typical for other TSRs as well, however it takes approximately half a revolution longer for the predictions to stabilize for lower TSRs where as mentioned before, flow separation prevails. The convergence behavior is also shown in the figures which again only partially satisfies the 10^{-6} acceptable threshold .

5.3 Cavitating Flow Analysis

The procedure for cavitating flow calculations is similar to the TSR diagrams with an additional multiphase stage in the end which is administered using four different numerical setups as demonstrated in Figure 3.9, except this time only one TSR is selected and used, thus no TSR diagrams for the cavitating case. The full blade root geometry is employed, the Hub Pitch Angle is increased to 25° and advance per timestep in decreased to 0.25^o.

Before cavitating simulations can be performed, a wetted flow solution is needed. This, similar to the Case A procedure consists of a steady wetted flow simulation followed by an unsteady wetted flow simulation. The single phase field solution needs to be reproduced for the cavitating conditions reported by experiments which is different than flow conditions that were used for the TSR diagrams. The solver inputs that have been successfully used for the simulations of Sections 5.1 and 5.2 are therefore reconfigured to correspond to the only TSR of the cavitating case. The cavitation-yielding conditions of interest as documented in Bahaj, Molland,

(a) TSR4   **(b)** TSR5   **(c)** TSR6   **(d)** TSR7   **(e)** TSR8
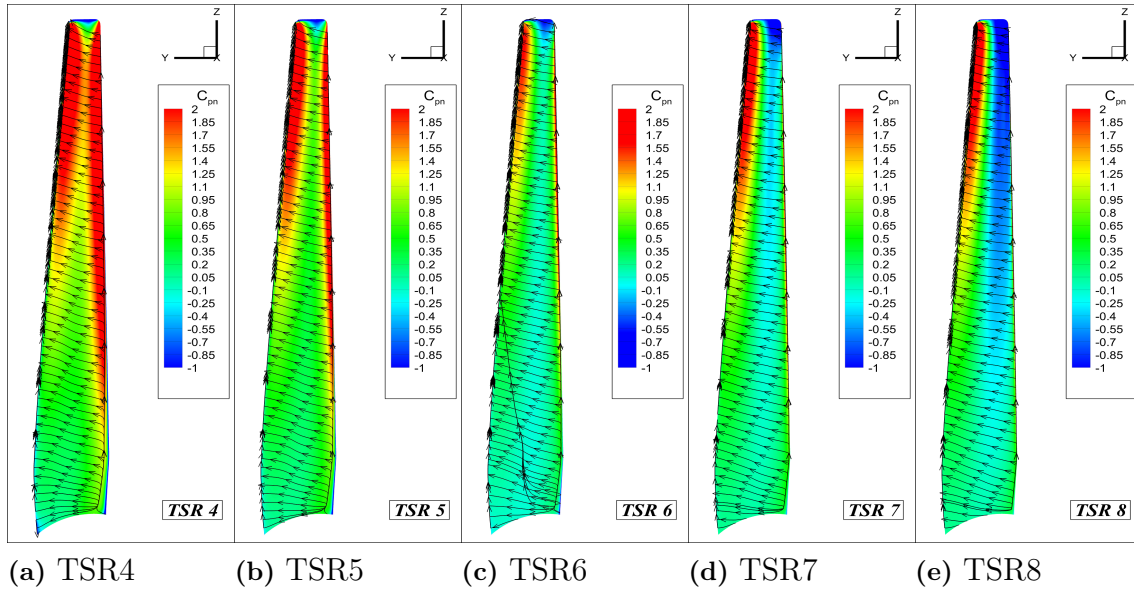
Figure 5.5: Pressure distribution and limiting streamlines for unsteady calculations, pressure side. $U_T = 1.73[m/s]$ and 20° Hub Pitch Angle using k-ω (SST-2003).

(a) TSR4   **(b)** TSR5   **(c)** TSR6   **(d)** TSR7   **(e)** TSR8
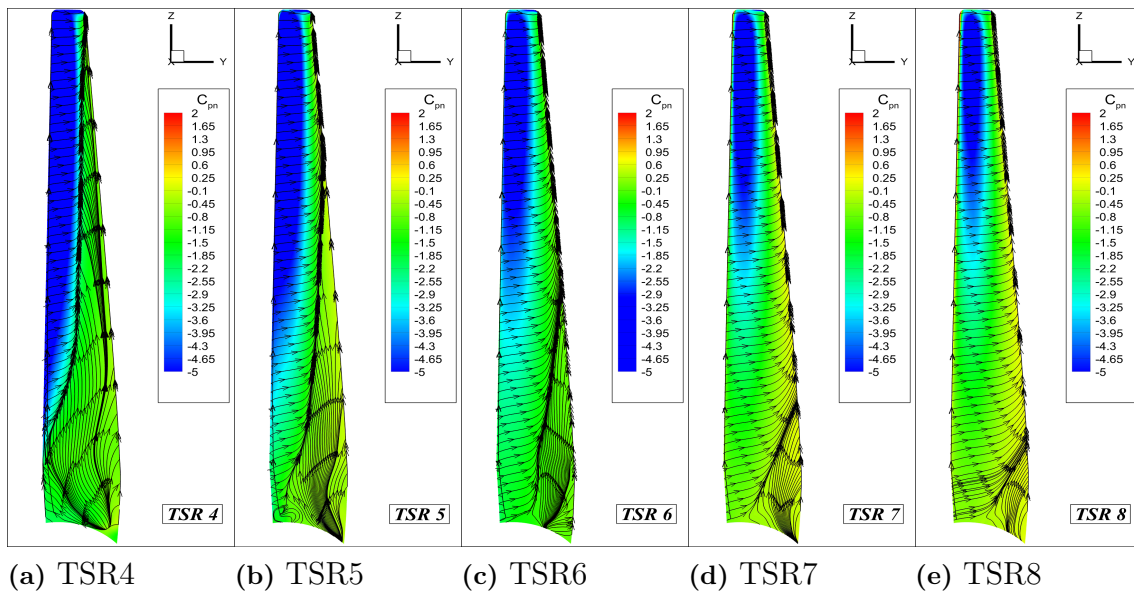
Figure 5.6: Pressure distribution and limiting streamlines for unsteady calculations, suction side. $U_T = 1.73[m/s]$ and 20° Hub Pitch Angle using k-ω (SST-2003).

45
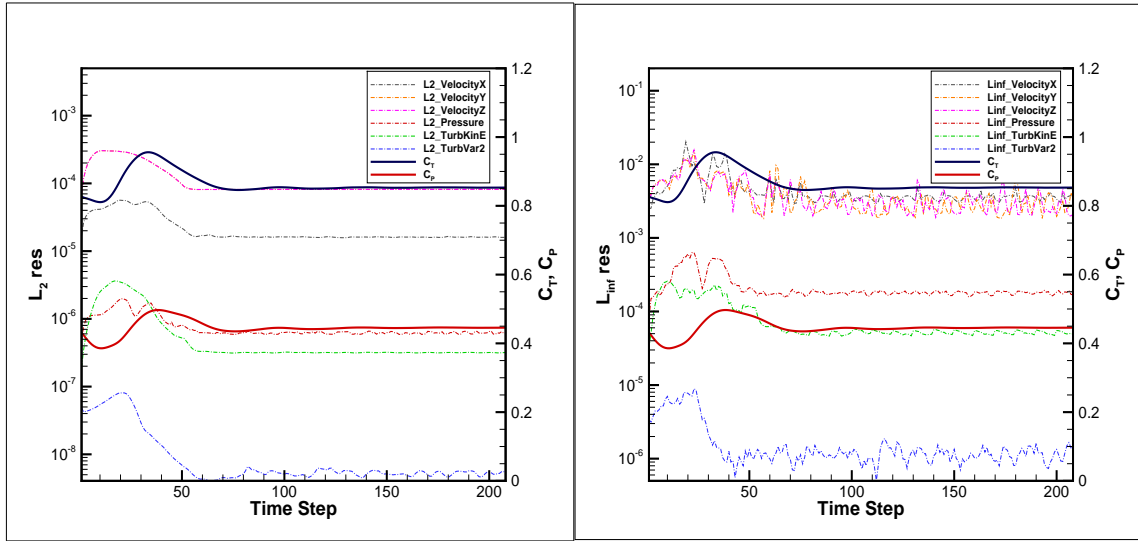
(a) L_2 Residual Norms

(b) L_∞ Residual Norms

Figure 5.7: Variation of thrust and power prediction with time, convergence behavior for unsteady calculations using KSKL at TSR=7.
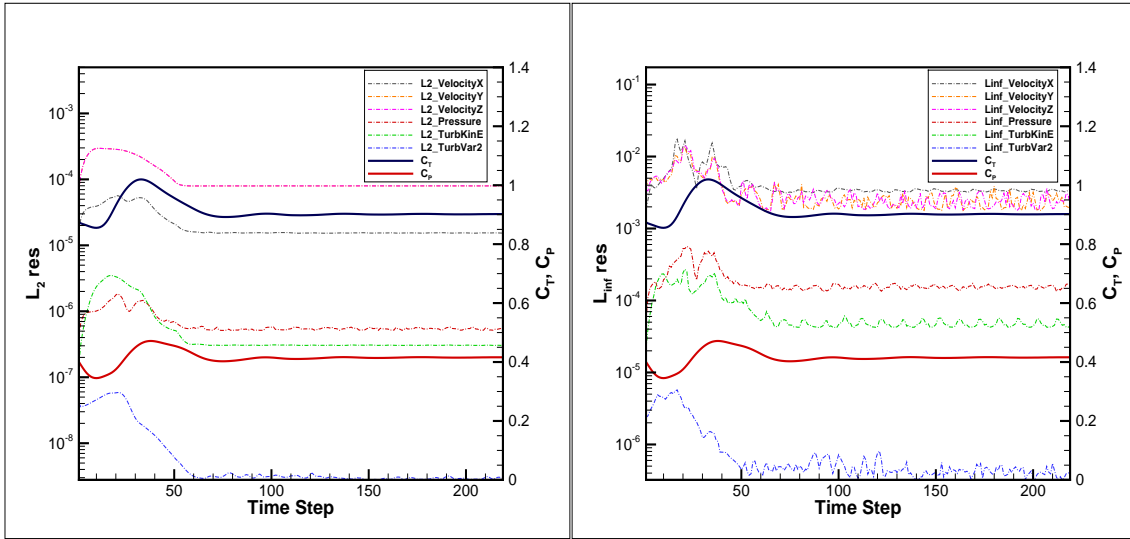
(a) L_2 Residual Norms

(b) L_∞ Residual Norms

Figure 5.8: Variation of thrust and power prediction with time, convergence behavior for unsteady calculations using KSKL at TSR=8.

et al. (2007) are turbine speed at 250 rpm, TSR=7.5, $V_{res} = 10.6$, $\sigma = 0.63$ and $23,000[N/m^2]$ tunnel side static pressure which resulted in a 15% partial sheet cavity over the blades suction side. .

Figures 5.11 and 5.12 show a comparison of the turbulent wake generation for the different turbulence models used. It is seen that k-ω (SST-2003) yields a larger turbulent wake compared with KSKL despite both models resulting in the almost identical flow separation mid-chord on the pressure side.

The same pattern is observed at a higher blade section at $0.7R$ blade radius
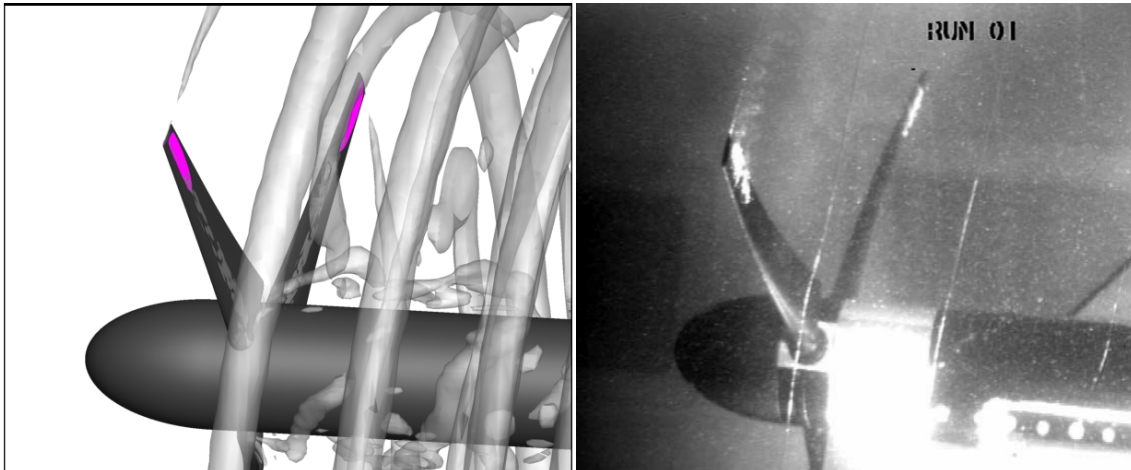
Figure 5.9: Left: 25° hub pitch angle, flow speed= $1.4[m/s]$, TSR=7.5, $\sigma = 0.63$. vapor volume fraction=0.1 highlighted in magenta, Q-criterion=1 highlighted in gray transparent iso-surfaces. Right: Cavitation tunnel high speed camera photography of the same case. Photograph courtesy of (Bahaj, Molland, et al., 2007) and University of Southampton.
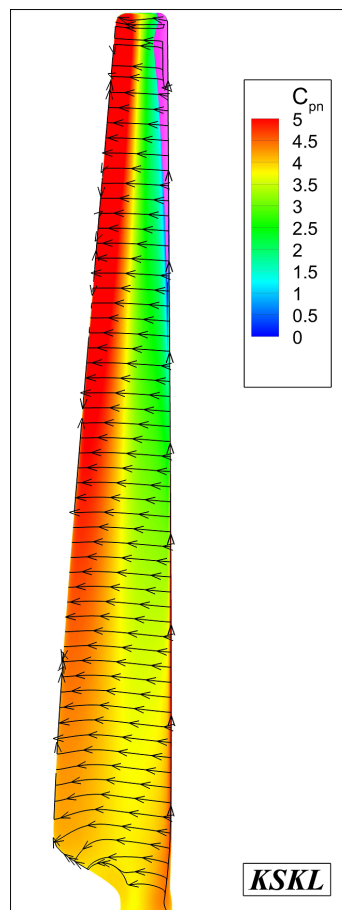
Figure 5.10: Pressure side cavity near blade tip at leading edge, 10% vapor volume fraction highlighted in magenta.

(a) Steady   **(b)** Unsteady   **(c)** Cavitating
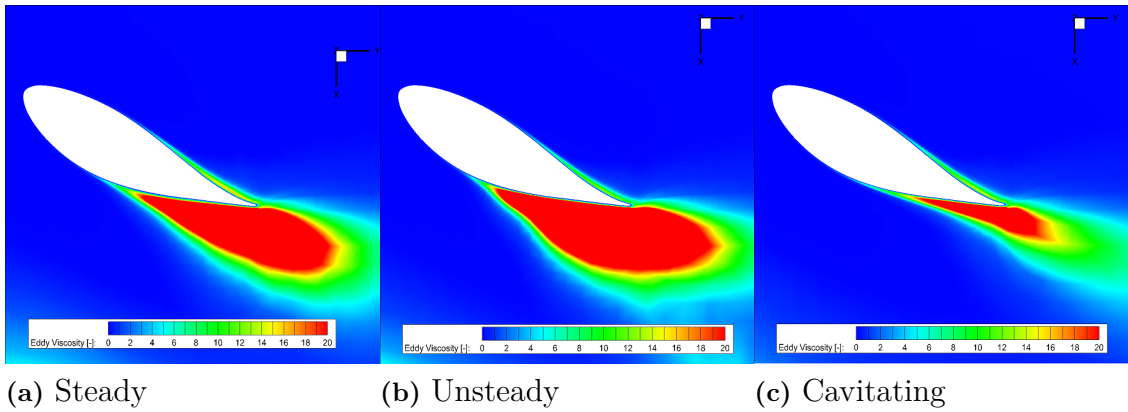
Figure 5.11: Turbulent wake generation in terms of eddy-viscosity non-dimensionalized for molecular viscosity. Blade section at $r/R = 0.2$ using KSKL turbulence model.

(a) Steady   **(b)** Unsteady   **(c)** Cavitating
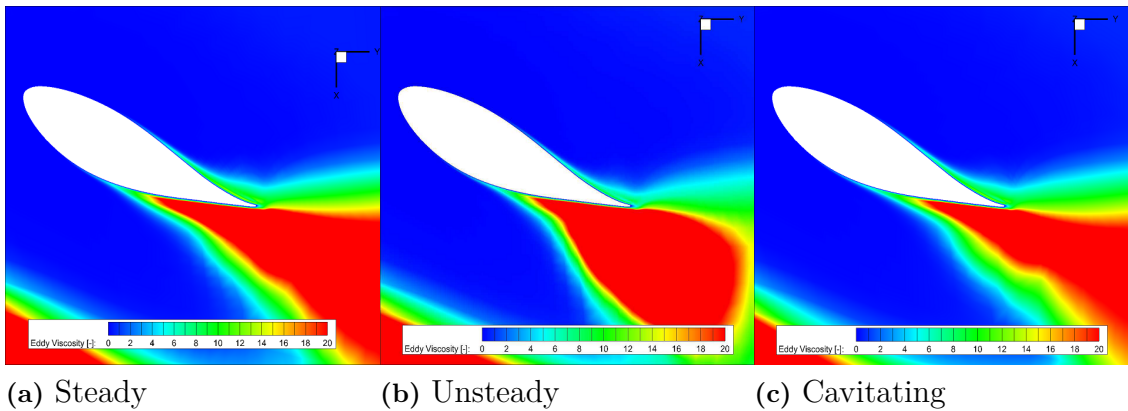
Figure 5.12: Turbulent wake generation in terms of eddy-viscosity non-dimensionalized for molecular viscosity. Blade section at $r/R = 0.2$ using k-ω (SST-2003) turbulence model.

going through the suction side cavity in Figures 5.13 and 5.14 where it is further observed that the presence of the cavity has an influence on turbulent viscosity contour morphology most visibly near the cavity closure line.

Flow visualization in Figure 5.15 for the two turbulence models at a blade section very close to the tip where both pressure and suction side cavities exist indicates that the cavity predictions are larger when using k-ω (SST-2003) once again contributing to the notion that cavitation is highly turbulence-sensitive. These cavity sections are investigated in more detail below where the effects of the Reboud correction are discussed.

The vortical field is visualized in Figure 5.16 with the pressure side cavity visible in the upstream view and the suction side cavity visible in the downstream view. The two turbulence models yield fairly identical results here and only results from k-ω are presented.

One way to observe the effect of turbine operation on the flow is to look at stream kinetic energy in the presence and absence of cavitation. As visualized in Figure

(a) Steady **(b)** Unsteady **(c)** Cavitating
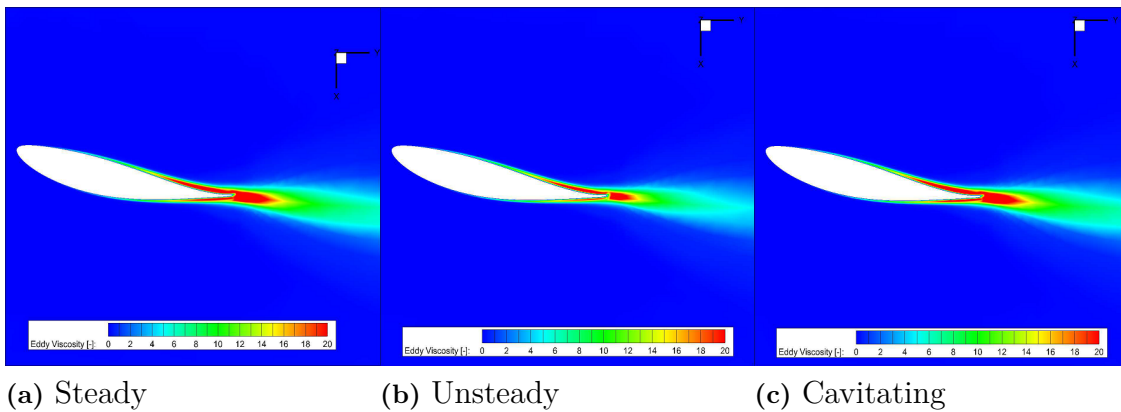
Figure 5.13: Turbulent wake generation in terms of eddy-viscosity non-dimensionalized for molecular viscosity. Blade section at $r/R = 0.7$ using KSKL turbulence model.


(a) Steady **(b)** Unsteady **(c)** Cavitating
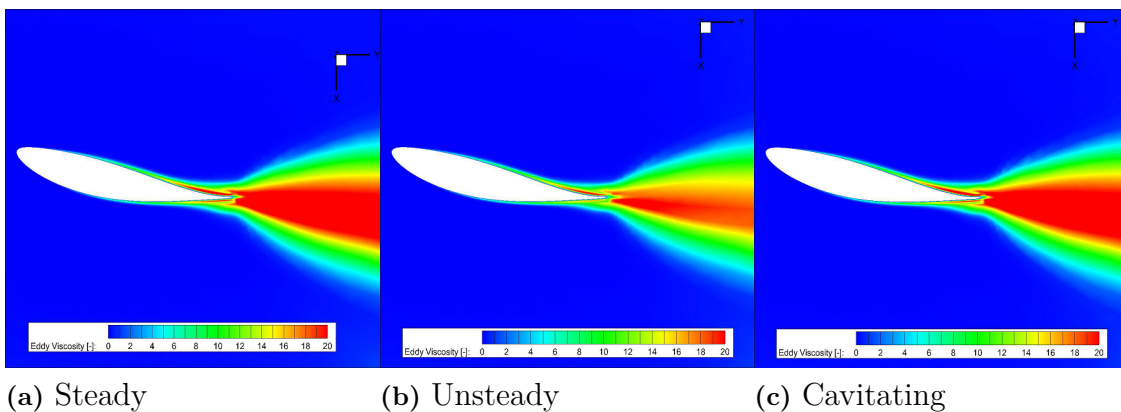
Figure 5.14: Turbulent wake generation in terms of eddy-viscosity non-dimensionalized for molecular viscosity. Blade section at $r/R = 0.7$ using k-ω (SST-2003) turbulence model.

5.17 multiple stagnation points exists throughout the flow most notably at the bow of the hub as well as aft of the hub and to a lesser visibility on the pressure side of the blades close to the root. Kinetic energy is here calculated based on the 3D velocity magnitude. Note that the images represent different timesteps as it is not possible to have cavitating and wetted flow at the same instance. This is because of the simulations workflow which always puts cavitating flow 2 revolutions after the wetted flow simulation is completed. The blade rotations are however selected so as to correspond to the same turbine position. There is no tangible difference observed from this comparison and the tip vortices are missing but the clockwise hub vortices are visible via the hot spots.

5.3.1 Cavity Dynamics and Shedding

The multiphase simulations result in similar sheet cavity coverage on the suction side compared with experiments, interestingly an additional partial sheet cavity near the

(a)   **(b)**
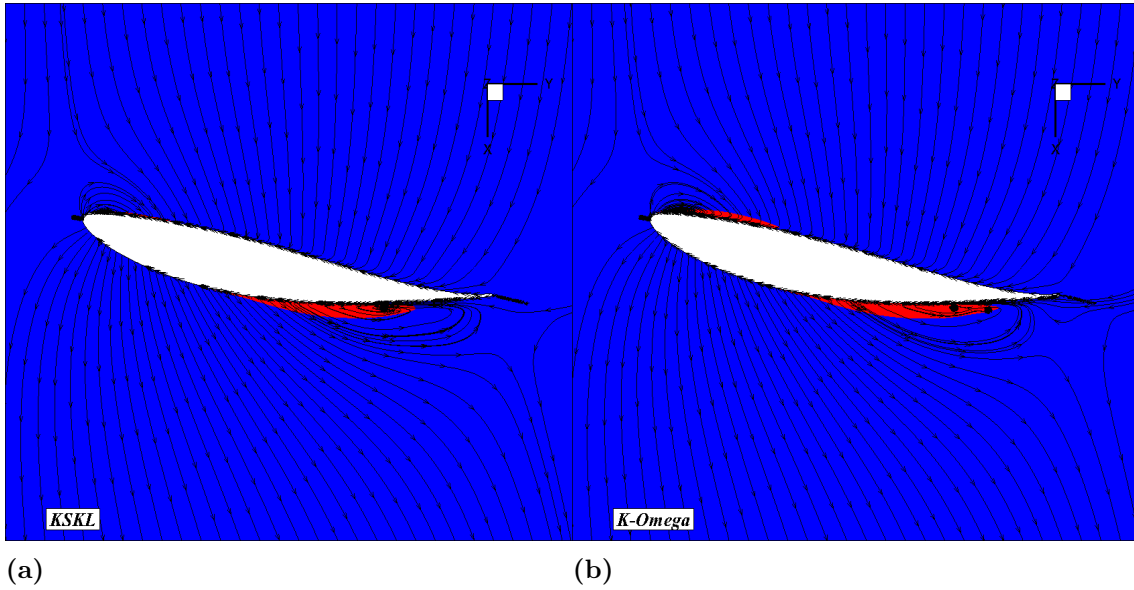
Figure 5.15: Model comparison for flow visualization using velocity streamlines and cavity prediction at $r/R = 0.95$ blade radius, with higher than 50% vapor volume fraction indicated in red.

leading edge of the pressure side is observed which was not previously reported by the experiments, see Figure 5.10.

Despite the fact that no cavity shedding has been reported by the experiments, inspection of the flow field in cavitating flow indicates properties which may be attributed to transient phenomena such as shedding of the partial cavity. Most notably the development of the horseshoe cavity structure points towards transient cavitation behavior.

A chord-based Strouhal number analysis shows that the selected timestep of 0.25^o is likely inadequate in capturing the developments of the re-entrant jet such as the rise time and cloud shedding. An acceptable Strouhal number corresponding to the periodic behavior of partial sheet cavity shedding is 0.3 describing a 30% rise time compared with the shedding period (Franc & Michel, 2006).

Based on the cavity extent as observed in Figure 5.20, the chord-wise cavity length at the maximum extent which is used as characteristic length is approximately 60% of the blade chord length. Using the resultant velocity at $r/R = 0.95$ from Equation (3.1) the Strouhal number as defined by

$$St = \frac{\nu L}{U} \tag{5.2}$$

with ν as shedding frequency, L as charcteristic length and U as characteristic velocity is set to 0.3 which gives a shedding period of 4.344E-3 seconds. This is the time it should take for a re-entrant jet in the order of mean flow to traverse the maximum extent of the partial cavity. As the timestep for calculations is set to 1.662E-3 seconds corresponding to a 0.25^o advance per timestep, it is concluded that temporal resolution is inadequate since best practices in ReFRESCO use a value of $T_{ref}/100$ as time advance where T_{ref} is the physical period.
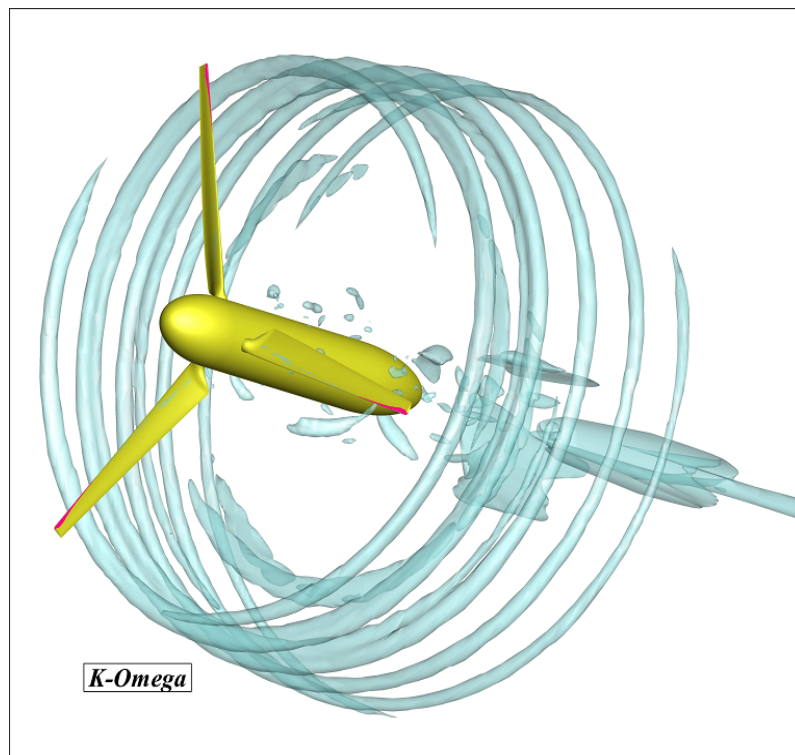
(a) Pressure Side
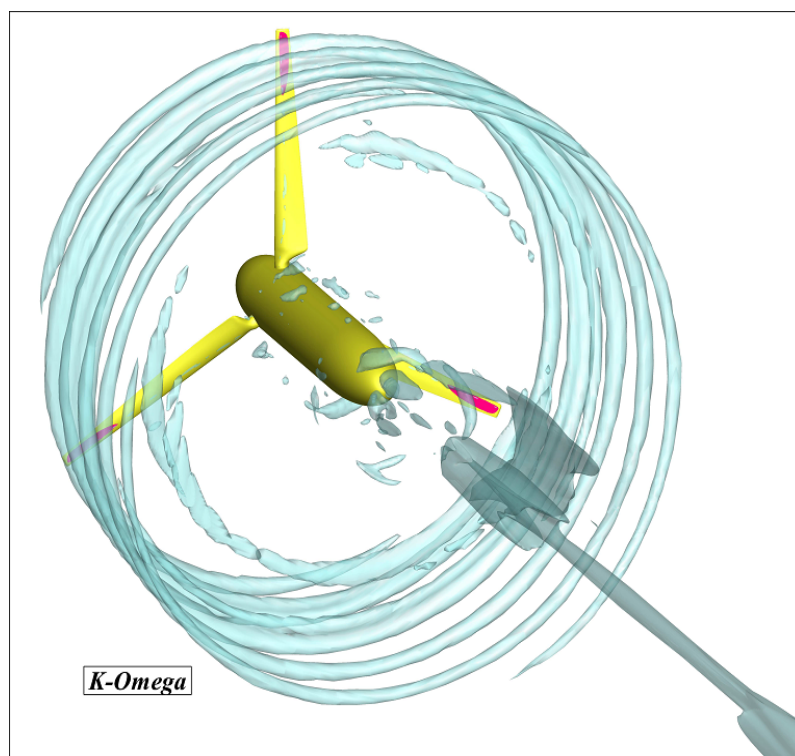
(b) Suction Side

Figure 5.16: Vortical field visualization via Q-Criterion=3, 10% vapor volume fraction shown in magenta.

(a) Wetted Flow
(b) Cavitating
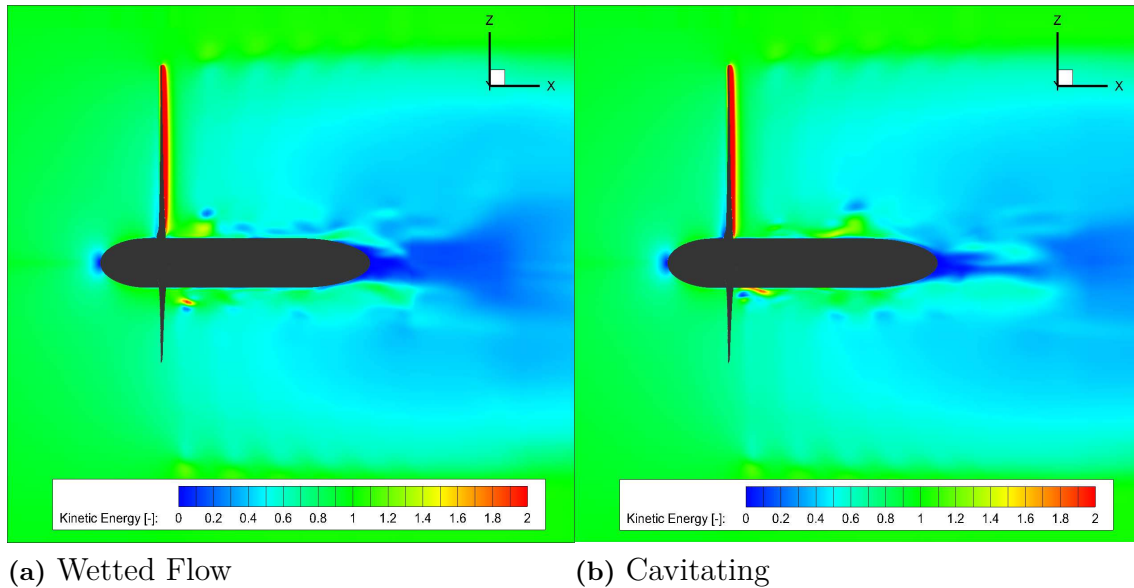
Figure 5.17: Flow kinetic energy non-dimensionalized by free stream kinetic energy, KSKL model.

As previously seen in Figure 5.15 the velocity streamlines that engulf the suction side cavity resemble the patterns of a re-entrant jet. Figure 5.18a inspects these patterns more closely, where it is seen that local velocity vectors form a span-wise vortex at the closure line of the cavity. The vorticity, when aligned with the span of the blade can be an indication of the re-entrant jet and the subsequent vapor shedding (Koop, 2008). It is verified that the vortex formation is not purely a result of the blade surface curvature when the non-cavitating flow is observed for the same blade section in Figure 5.18b.

In addition to the observation that total vapor coverage is hardly sensitive to time (Figure 5.19), it is also of interest to determine whether the blades position has any effect on the generated amount of vapor. To that end a single blade is picked out and monitored for vapor fraction variations in Figure 5.20 as it completes one revolution. It should be noted that the indicated timesteps on their own are not important but the difference between the timesteps indicates the relative position of the blade throughout a revolution, where each timestep equals a 0.25^o advance. The same blade loading variations are observed for both turbulence models thus switching from one set of data to the other is understood not to harm the coherence of the analysis, at least on the subject of interest here. The onset of a possible re-entrant jet can be identified through the streamtraces that are approaching the cavity closure line along the span. No noticable change is seen in the coverage or structure of the cavity iso-surface. Streamlines appear to be constant with time nearer to the tip. Close to the hub connection however there appears to exist a transient vortex but the vortex exits the blade surface far away from the major sheet cavity formation[1]. The constant pressure distribution, streamlines and cavity volume can be contributed to

---

[1]These blade root turbulent vortices reported in Otto, Rijpkema, and Vaz (2012) were the reason for modifying the cylindrical connection geometry.
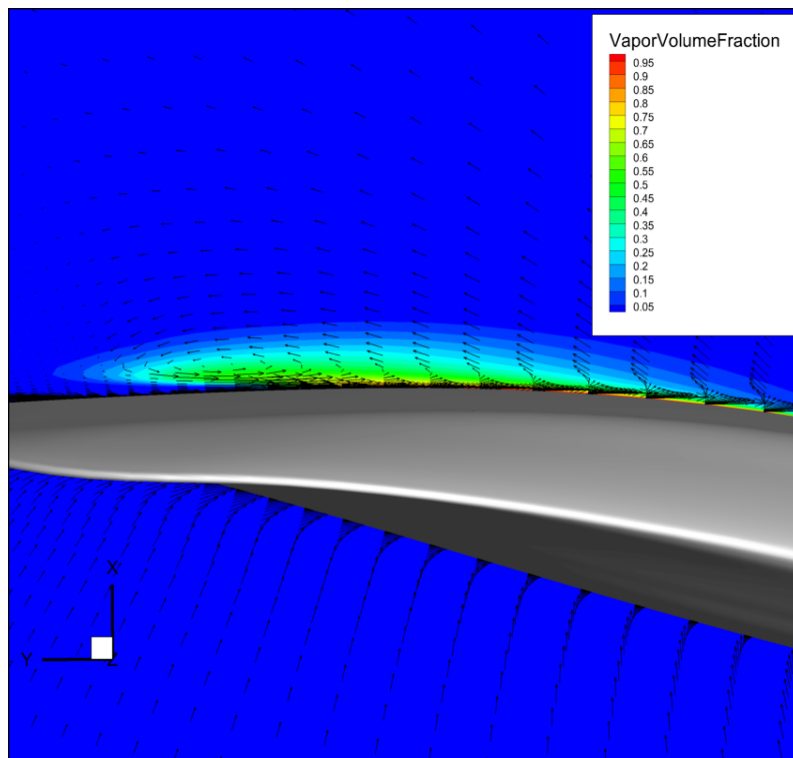
(a)
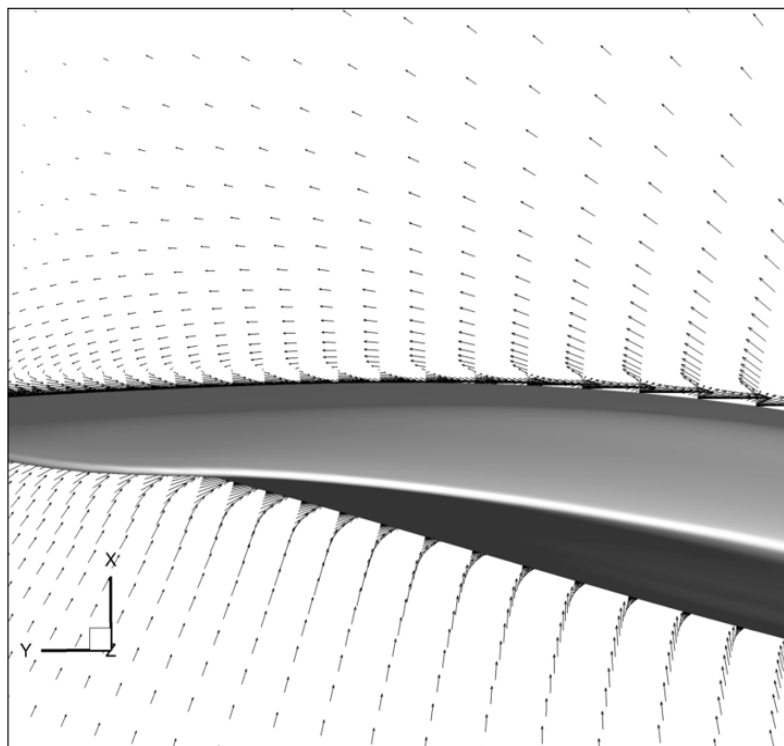
(b)

Figure 5.18: Vorticity in and around the suction-side cavity region (a) cavitating flow, (b) wetted flow.

the omitting of gravity effects i.e., as far as the blade pressure is concerned there is no difference between the top and bottom of a revolution cycle, especially since the inflow has uniform conditions. However the loss of cavitation dynamics is not due to this, the smooth outline of the cavity iso-surfaces hint towards the need for higher cell refinement near the cavitation susceptible regions which can be one important reason behind the static presence of the cavity. In an effort to "liven up" the vapor region the Reboud correction is applied to the flow.
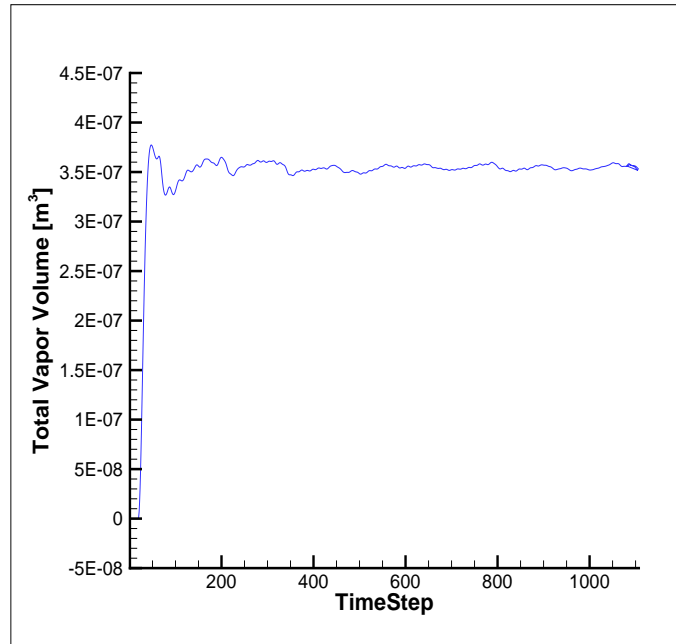

Figure 5.19: Vapor volume variation with time, k-ω (SST-2003).

5.3.2 Eddy-Viscosity Correction

It was earlier suggested that incompressible RANS simulations may after all be inadequate in capturing the dynamics of cavitation. A proper improvement strategy would be to increase mesh density at the cavity region and perhaps even use finer timesteps, but since these operations require considerably greater time and computational resources a more readily available method is employed.

The Reboud correction as previously explained in Section 2.4 is used to decrease the viscosity near the cavitating regions in order to allow for the vapor to more easily be influenced by flow momentum. Initially the highest Reboud damping factor for ReFRESCO was used but this resulted in numerical instability. Consequently the damping factor was switched to a very low value of (n=1) against recommendations by the original author as seen in Equation (2.24). In similar application such as the work of Li et al., (2010), n values as high as 100 have been used and ReFRESCO does not impose any limitations on the parameter, however in the original definitions values close to 9 have been suggested by Coutier-Delgosha et al., (2003).

Figure 5.21 revisits the vorticity in and around the suction-side cavity from Figure 5.18 with the Reboud correction applied. A closer view of the velocity field
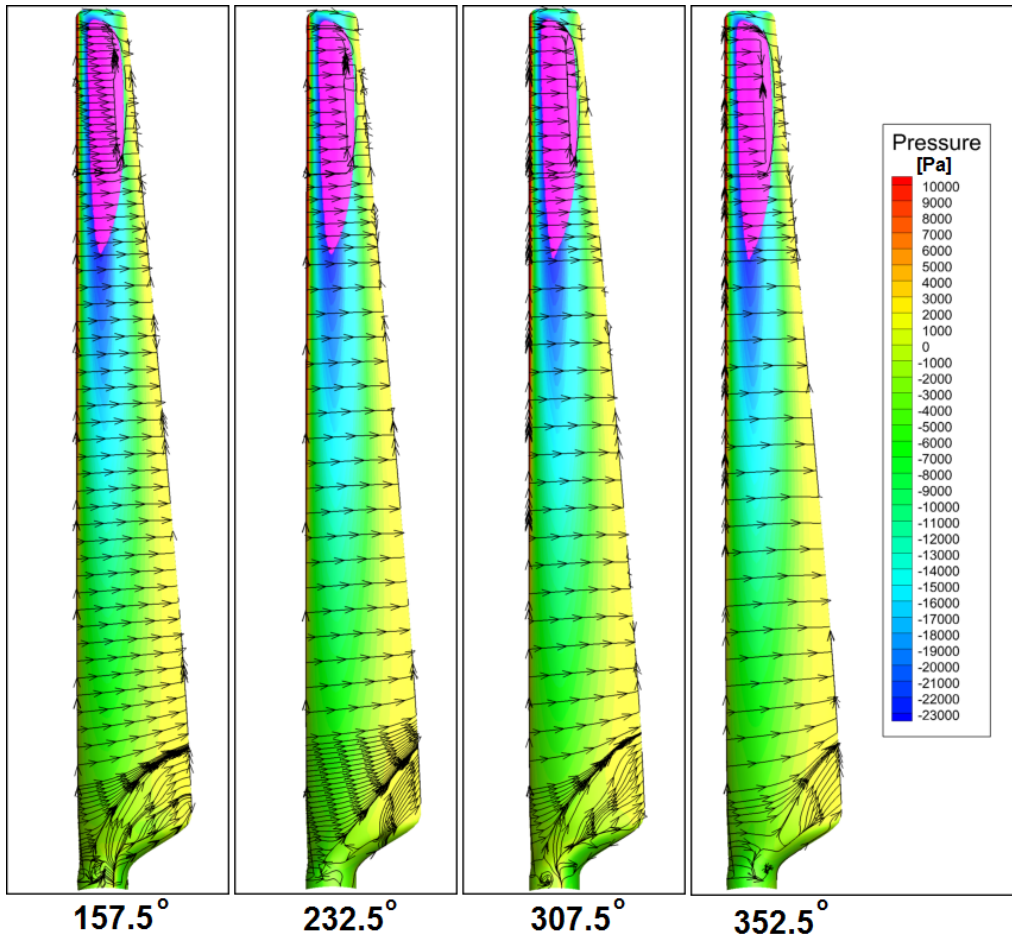
Figure 5.20: Suction side of a single blade at various deflection angles as it completes one revolution. 10% vapor volume fraction highlighted in magenta, KSKL model.

surrounding the vapor-liquid interface and more importantly at the cavity-blade interface towards the trailing edge reveals that vorticity is now modified and velocity vectors near to the cavity-blade interface have been intensified. This is to be expected of the eddy-viscosity correction, however the vector magnitudes are still small and can not result in a fully extended re-entrant jet that would reach the entire chord-wise length of the cavity. The eddy-viscosity was also observed to be identical at the slices where it was previously observed, images are omitted to prevent repetitiveness. It becomes interesting then to determine what causes the correction to not yield the expected shedding or detaching response.

Figure 5.22 shows three of the possible n values that can be used to employ the Reboud correction. Value of $n = 1$ corresponds to the case mentioned above. An iso-line for the 10% vapor volume fraction values is plotted which should serve to indicate a reasonable cavity boundary for our purposes. The intensity of the Reboud correction factor is increased with higher values of n. It is found that the region of influence of the correction barely reaches the boundary of the cavity, which is the area where most dynamic activities are expected, even for the intermediate value of $n = 5$. Only at $n = 10$ does the maximum effective region of the eddy-viscosity
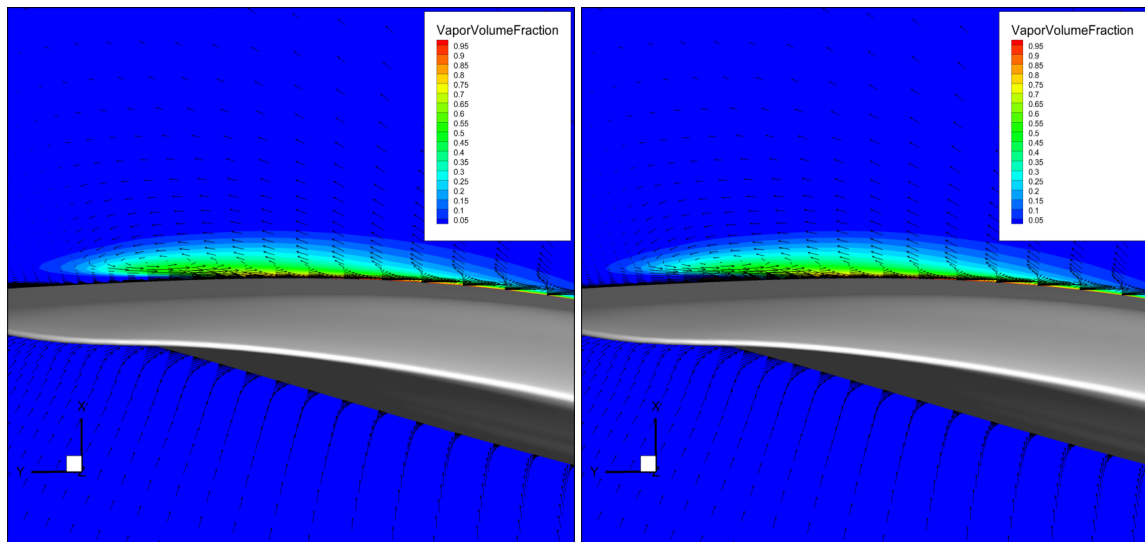
(a) Original cavitation model.　　　　**(b)** Reboud correction model.

Figure 5.21: Effect of Reboud correction with $n = 1$ turbulent viscosity damping on the velocity field.

reduction factor reach the closure line of the cavity where one would expect the re-entrant jet to develop. For smaller n values the correction will only influence regions with very high vapor volume fractions close to 1 which in the present case lie in the center of the chord-wise extent of the cavity. This is identified as the reason why applying the eddy-viscosity correction has not been fruitful in adding dynamics to the cavity formation and suggests that low values for n are not effective.
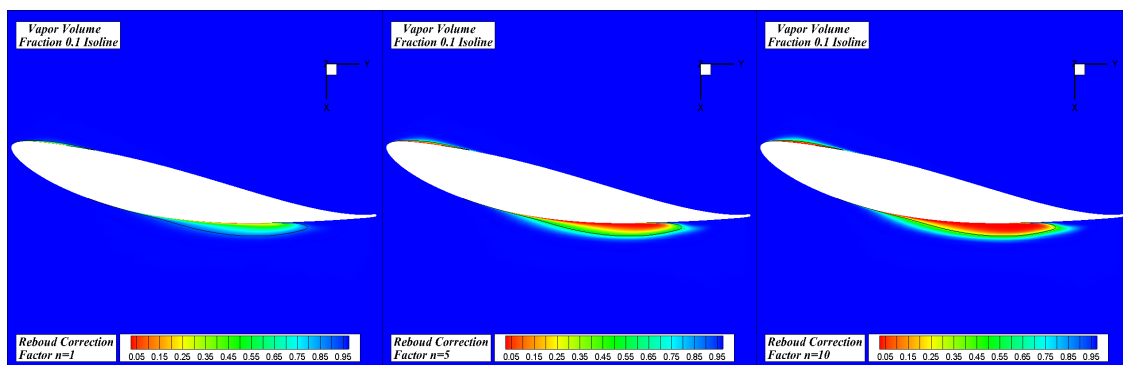
(a) $n = 1$　　　　　**(b)** $n = 5$　　　　　**(c)** $n = 10$

Figure 5.22: Role of value n in Reboud correction influence over the vapor region.

6

Conclusions and Future Work

6.1 Conclusions

The single benchmark case of interest for this thesis is presented in Figure 5.9. As far as reproducing the flow goes the results are quite satisfying. Since there is very little quantitative data available for the experimental case of the high speed photograph it can be problematic to investigate the flow for validation reasons. However with regards to vortex identification and low pressure regions detection the comparison is satisfactory and it is concluded that the basis for consequent investigations into the test case have been successfully established. The numerical methodology used for vortex identification was briefly described in Section 2.6. It is fairly straight forward from this point on to perform URANS studies on this case and possibly similar geometries using ReFRESCO.

- It is observed that the steady case at TSR=4 compares poorly against experimental values even when a converged solution is reached, but the unsteady wetted simulations based on those steady solutions improve with time and approach the experimental values quite easily.

- The uncertainty analysis revealed the largest numerical errors to be associated with low TSR values where large flow separation is observed. The simulations ability to capture transitional flow may thus need to be improved.

- The use of two turbulence models in most cases yield similar results. One exception is the generated wake turbulence which for k-ω (SST-2003) is found to be greater than k-$\sqrt{k}L$.

- A sheet cavity is observed at the position where it was generated in the experiments and similar in shape. It is found to be a steady formation and shedding or other transformations are not captured. This is attributed to the lack of resolution in space and time or the Reynold's averaged methods inability to resolve highly transient phenomena accurately.

- Evidence for existence of a re-entrant jet (velocity vectors) seem to suggest that the flow field is resolved with adequate resolution to capture the hydrodynamic effects of a vapor cavity but the simulation lacks both spacial and temporal resolution that is required to resolve the evolution of these multiphase hydrodynamics with time, rendering it in a seemingly steady manner when in fact there seems to exist a shedding mechanism.

- Use of eddy-viscosity correction is unsuccessful in improving cavity dynamics which is investigated and found to be the result of low n values in addition to lack of spacial resolution.

- Use of steady simulations on the coarse mesh delivers satisfactory results if only the pressure field is of interest, from which an extent prediction for the cavity is also possible. If however unsteady cavity dynamics are of interest, the use of refined cells at the cavity closure line and possibly at the location of cloud shedding is required.

6.2 Future Work

What started as a simple list of objectives has grown into a platform for multiple future developments.

- The grid resolution used in cavitating simulations is found to be inadequate for capturing dynamic behavior of the cavities and is thus required to increase for future attempts.

- Effects of gravitational acceleration which in turn influences the density gradient, could be a subject of further investigation. Additionally the free surface effects and possibly an array of different wave conditions could be of interest since the varying wave height can in fact modify cavitating behavior specifically at the blade tips when they are close to the water surface with minimal hydrostatic pressure and mixing between the air and water.

- Restricted flow can be introduced via redefining the computational domain to resemble the dimension of the actual cavitation tunnel in the experiments.

- Cases contained herein are entirely performed at Reynold's numbers corresponding to model scale conditions. As the Reynold's numbers increase to the full scale, the flow regime undergoes significant changes (Otto et al., 2012). Due to the fully developed turbulent nature of these flow regimes it is for practical purposes suggested that the research be extended to full scale Reynold's numbers in order to obtain an accurate, realistic understanding of the cavitation behavior of the full scale turbines.

- A local refinement of the computational grid in regions where cavities are detected as well as employment of compressible RANS equations may prove to aid the capturing of cavitation dynamics and collapse mechanisms.

- Extending the cavitating cases to the entire TSR range is another possible beneficial development. It would be interesting (if not crucial) to demonstrate one non-cavitating case to ensure reliability of the results obtained and methods used herein.

- A parametric study on initial nuclei count and radii is of interest in order to obtain an understanding of the relevance of the cavitation model.

- For a more comprehensive verification study the inclusion of a 5th grid could further enhance the convergence of the C_T curves and is subject to future work. The cavitating simulation can also undergo a grid refinement study.

References

Afgan, I., McNaughton, J., Rolfo, S., Apsley, D., Stallard, T., & Stansby, P. (2013). Turbulent flow and loading on a tidal stream turbine by les and rans. *International Journal of Heat and Fluid Flow*, *43*, 96–108.

Ahuja, V., Hosangadi, A., & Arunajatesan, S. (2001). Simulations of cavitating flows using hybrid unstructured meshes. *Journal of Fluids Engineering*, *123*(2), 331–340.

Bahaj, A., Batten, W., & McCann, G. (2007). Experimental verifications of numerical predictions for the hydrodynamic performance of horizontal axis marine current turbines. *Renewable Energy*, *32*(15), 2479–2490.

Bahaj, A., Molland, A., Chaplin, J., & Batten, W. (2007). Power and thrust measurements of marine current turbines under various hydrodynamic flow conditions in a cavitation tunnel and a towing tank. *Renewable energy*, *32*(3), 407–426.

Bahaj, A., & Myers, L. (2003). Fundamentals applicable to the utilisation of marine current turbines for energy production. *Renewable energy*, *28*(14), 2205–2211.

Banks, J., Bercin, K., Lloyd, T. P., & Turnock, S. R. (2013). Fluid structure interaction analyses of tidal turbines.

Batten, W., Bahaj, A., Molland, A., & Chaplin, J. (2008). The prediction of the hydrodynamic performance of marine current turbines. *Renewable energy*, *33*(5), 1085–1096.

British Petroleum. (2014). BP Energy Outlook 2035. *BP stats, Jan.*

Byrne, C. B. B., Cherrett, W., Grosvenor, R. I., Mason-Jones, A., Morris, C. E., O'Doherty, D. M., . . . Prickett, P. W. (2011). An investigation into the possible effects of cavitation on a horizontal axis tidal turbine.

Carbon Trust. (2011). Accelerating marine energy. *Carbon Trust Marine Energy Accelerator*.

Coutier-Delgosha, O., Fortes-Patella, R., & Reboud, J.-L. (2003). Evaluation of the turbulence model influence on the numerical simulations of unsteady cavitation. *Journal of Fluids Engineering*, *125*(1), 38–45.

Davidson, L. (2011). Fluid mechanics, turbulent flow and turbulence modeling. *Chalmers University of Technology, Goteborg, Sweden (Nov 2011)*.

Eça, L., Vaz, G., & Hoekstra, M. (2010a). Code verification, solution verification and validation in rans solvers. In *Asme 2010 29th international conference on ocean, offshore and arctic engineering* (pp. 597–605).

Eça, L., Vaz, G., & Hoekstra, M. (2010b). A verification and validation exercise for the flow over a backward facing step. In *Proceedings of the eccomas cfd.*

Elghali, B., Eddine, S., Balme, R., Saux, K. L., Benbouzid, M. E. H., Charpentier,

J. F., & Hauville, F. (2007). A simulation model for the evaluation of the electrical power potential harnessed by a marine current turbine. *Oceanic Engineering, IEEE Journal of*, *32*(4), 786–797.

EMEC. (2015). *Tidal devices.* Retrieved from `http://www.emec.org.uk/marine-energy/tidal-devices/`

ESRU. (2006). *Marine current resource and technology methodology. background: Marine current energy.* Retrieved from `http://www.esru.strath.ac.uk/EandE/Web_sites/05-06/marine_renewables/background/marinecurrents.htm` (Accessed on 2015-11-16)

Flumill AS. (2012). *Flumill, the technology.* Retrieved from `http://www.flumill.com/The_Technology/content-1.html` (Accessed on 2015-11-16)

Franc, J.-P., & Michel, J.-M. (2006). *Fundamentals of cavitation* (Vol. 76). Springer Science & Business Media.

Hardisty, J. (2008). Power intermittency, redundancy and tidal phasing around the united kingdom. *The Geographical Journal*, *174*(1), 76–84.

Harris, A. (2012). *Tidal energy comes of age.* Retrieved from `http://eandt.theiet.org/magazine/2012/12/taming-the-tides.cfm` (Accessed on 2015-11-16)

Hirt, C. W., & Nichols, B. D. (1981). Volume of fluid (vof) method for the dynamics of free boundaries. *Journal of computational physics*, *39*(1), 201–225.

Hoekstra, M., & Vaz, G. (2009). The partial cavity on a 2d foil revisited.

Holmén, V. (2012). Methods for vortex identification. *Master's Theses in Mathematical Sciences*.

Huang, B., Kanemoto, T., et al. (2015). Numerical simulation for cavitation around horizontal-axis counter-rotating type propellers in a tidal stream power unit (in preparation for suppressing cavitation). In *The twenty-fifth international offshore and polar engineering conference.*

Klaij, C., & Vuik, C. (2013). Simple-type preconditioners for cell-centered, colocated finite volume discretization of incompressible reynolds-averaged navier–stokes equations. *International Journal for Numerical Methods in Fluids*, *71*(7), 830–849.

Kolář, V. (2007). Vortex identification: New requirements and limitations. *International journal of heat and fluid flow*, *28*(4), 638–652.

Koop, A. H. (2008). *Numerical simulation of unsteady three-dimensional sheet cavitation.* University of Twente.

Kunz, R. F., Boger, D. A., Stinebring, D. R., Chyczewski, T. S., Lindau, J. W., Gibeling, H. J., . . . Govindan, T. (2000). A preconditioned navier–stokes method for two-phase flows with application to cavitation prediction. *Computers & Fluids*, *29*(8), 849–875.

Lampe, A. (2015). *RENT; Viscous Flow Computations on Southampton Current Turbine* (Tech. Rep. No. 70050-3-RD). MARIN.

Lee, J. H., Park, S., Kim, D. H., Rhee, S. H., & Kim, M.-C. (2012). Computational methods for performance analysis of horizontal axis tidal stream turbines. *Applied Energy*, *98*, 512–523.

Li, D.-q., Grekula, M., & Lindell, P. (2010). Towards numerical prediction of unsteady sheet cavitation on hydrofoils. *Journal of Hydrodynamics, Ser. B*, *22*(5), 741–746.

62

Lloyd, T. P., Turnock, S. R., & Humphrey, V. F. (2011a). Modelling techniques for underwater noise generated by tidal turbines in shallow waters. In *Asme 2011 30th international conference on ocean, offshore and arctic engineering* (pp. 777–785).

Lloyd, T. P., Turnock, S. R., & Humphrey, V. F. (2011b). Unsteady cfd of a marine current turbine using openfoam with generalised grid interface.

Make, M., & Vaz, G. (2015). Analyzing scaling effects on offshore wind turbines using cfd. *Renewable Energy*, *83*, 1326–1340.

Mcnaughton, J. (2013). Turbulence modelling in the near-field of an axial flow tidal turbine in code_saturne.

McNaughton, J., Afgan, I., Apsley, D., Rolfo, S., Stallard, T., & Stansby, P. (2014). A simple sliding-mesh interface procedure and its application to the cfd simulation of a tidal-stream turbine. *International Journal for Numerical Methods in Fluids*, *74*(4), 250–269.

MCT. (2011). *Marine current turbines kicks off first tidal array for wales.* Retrieved from `http://www.marineturbines.com/3/news/article/44/marine_current_turbines_kicks_off_first_tidal_array_for_wales` (Accessed on 2015-11-16)

Menter, F., Kuntz, M., & Langtry, R. (2003). Ten years of industrial experience with the sst turbulence model. *Turbulence, heat and mass transfer*, *4*(1).

Menter, F. R., Egorov, Y., & Rusch, D. (2006). Steady and unsteady flow modelling using the k-kl model. *ICHMT DIGITAL LIBRARY ONLINE*, *10*.

Minesto AB. (2011). *Deep green technology.* Retrieved from `http://minesto.com/deep-green/` (Accessed on 2015-11-16)

Moser, J. (1978). Is the solar system stable? *The Mathematical Intelligencer*, *1*(2), 65–71.

Otto, W., Rijpkema, D., & Vaz, G. (2012). Viscous-flow calculations on an axial marine current turbine. In *Asme 2012 31st international conference on ocean, offshore and arctic engineering* (pp. 369–382).

Reboud, J., Coutier-Delgosha, O., Pouffary, B., & Fortes-Patella, R. (2003). Numerical simulation of unsteady cavitation flows: Some applications and open problems. In *Fifth international symposium on cavitation* (pp. 1–10).

Rijpkema, D., & Vaz, G. (2011). Viscous flow computations on propulsors: verification, validation and scale effects. *Proceedings of the Developments in Marine CFD*.

Sauer, J., & Schnerr, G. (2001). Development of a new cavitation model based on bubble dynamics. *ZAMM-Journal of Applied Mathematics and Mechanics/Zeitschrift für Angewandte Mathematik und Mechanik*, *81*(S3), 561–562.

Şenocak, I. (2002). *Computational methodology for the simulation of turbulent cavitating flows* (Unpublished doctoral dissertation). University of Florida.

Shi, W., Atlar, M., Norman, R., Aktas, B., & Turkmen, S. (2015). Biomimetic improvement for a tidal turbine blade.

Singhal, A. K., Athavale, M. M., Li, H., & Jiang, Y. (2002). Mathematical basis and validation of the full cavitation model. *Journal of fluids engineering*, *124*(3), 617–624.

Tidal Energy Today. (2015a). *Tocardo installs 5 tidal turbines.* Retrieved from

http://tidalenergytoday.com/2015/09/25/tocardo-installs-5-tidal
-turbines/ (Accessed on 2015-11-16)

Tidal Energy Today. (2015b). *Tocardo to install 5 tidal turbines in western netherlands.* Retrieved from http://tidalenergytoday.com/2015/06/16/tocardo-to-install-5-tidal-turbines-in-western-netherlands/ (Accessed on 2015-11-16)

Toxopeus, S., & Vaz, G. (2009). Calculation of current or manoeuvring forces using a viscous-flow solver. In *Asme 2009 28th international conference on ocean, offshore and arctic engineering* (pp. 717–728).

Turnock, S. R., Phillips, A. B., Banks, J., & Nicholls-Lee, R. (2011). Modelling tidal current turbine wakes using a coupled rans-bemt approach as a tool for analysing power capture of arrays of turbines. *Ocean Engineering*, *38*(11), 1300–1307.

Vaz, G., & Hoekstra, M. (2006). *Theoretical and numerical formulation of fresco code* (Tech. Rep.). Tech. Rep. 18572-WP4-2, MARIN, February.

Vaz, G., Jaouen, F., & Hoekstra, M. (2009). Free-surface viscous flow computations: Validation of urans code fresco. In *Asme 2009 28th international conference on ocean, offshore and arctic engineering* (pp. 425–437).

Versteeg, H. K., & Malalasekera, W. (2007). *An introduction to computational fluid dynamics: the finite volume method.* Pearson Education.

Wang, D., Atlar, M., & Sampson, R. (2007). An experimental investigation on cavitation, noise, and slipstream characteristics of ocean stream turbines. *Proceedings of the Institution of Mechanical Engineers, Part A: Journal of Power and Energy*, *221*(2), 219–231.

Yakhot, V., Orszag, S., Thangam, S., Gatski, T., & Speziale, C. (1992). Development of turbulence models for shear flows by a double expansion technique. *Physics of Fluids A: Fluid Dynamics (1989-1993)*, *4*(7), 1510–1520.

Zou, L., & Larsson, L. (2014). Cfd verification and validation in practice-a study based on resistance submissions to the gothenburg 2010 workshop on numerical ship hydrodynamics. In *30th symposium on naval hydrodynamics, hobart, australia.*